Diplomarbeit

Modeling and Simulation of Wetting and Icing on Laser-Structured Surfaces

ausgeführt zum Zwecke der Erlangung des akademischen Grades eines Diplom-Ingenieurs (Dipl.-Ing. oder DI) eingereicht an der TU Wien, Fakultät für Maschinenwesen und Betriebswissenschaften, von

Laszlo VÖRÖS

Matr.Nr.: 12130512

unter der Leitung von

Univ.Prof. Dipl.-Phys. Dr.-Ing. Andreas Otto
Institut für Fertigungstechnik und Photonische Technologien, E311

und

Dipl.-Ing. Constantin Zenz
Institut für Fertigungstechnik und Photonische Technologien, E311

Wien, Februar 2025

[redacted]

Unterschrift

Diese Arbeit wurde von FFG - Österreichische Forschungsförderungsgesellschaft im Rahmen des Programms "Take Off" (Projektnummer 43317863) unterstützt.

Ich nehme zur Kentniss, dass ich zur Drucklegung dieser Arbeit nur mit Bewilligung der Prüfungskommision berechtigt bin.

Eidesstattliche Erklärung

Ich erkläre an Eides statt, dass die vorliegende Arbeit nach den anerkannten Grundsätzen für wissenschaftliche Abhandlungen von mir selbstständig erstellt wurde. Alle verwendeten Hilfsmittel, insbesondere die zugrunde gelegte Literatur, sind in dieser Arbeit genannt und aufgelistet. Die aus den Quellen wörtlich entnommenen Stellen, sind als solche kenntlich gemacht.

Das Thema dieser Arbeit wurde von mir bisher weder im In- noch Ausland einem_r Beurteiler_in zur Begutachtung in irgendeiner Form als Prüfungsarbeit vorgelegt. Diese Arbeit stimmt mit der von den Begutachter_innen beurteilten Arbeit überein.

Ich nehme zur Kenntnis, dass die vorgelegte Arbeit mit geeigneten und dem derzeitigen Stand der Technik entsprechenden Mitteln (Plagiat-Erkennungssoftware) elektronisch-technisch überprüft wird. Dies stellt einerseits sicher, dass bei der Erstellung der vorgelegten Arbeit die hohen Qualitätsvorgaben im Rahmen der geltenden Regeln zur Sicherung guter wissenschaftlicher Praxis „Code of Conduct“ an der TU Wien eingehalten wurden. Zum anderen werden durch einen Abgleich mit anderen studentischen Abschlussarbeiten Verletzungen meines persönlichen Urheberrechts vermieden.

Wien, 25.02.2025
....
Ort und Datum

[redacted]
Unterschrift

Acknowledgements

I am profoundly grateful to my advisor, Prof. Andreas Otto, for his enduring support throughout this project. His expertise in the field of multiphase physics greatly enriched my work.

I extend my deepest gratitude to my co-advisor, Constantin Zenz, for the guidance and advice he provided me during the research. His insights, constructive feedback and essential suggestions have been invaluable for my thesis. I would also like to thank him for the commitment he has shown at every stage of the work.

I would like to thank Roland Fürbacher for sharing his knowledge with me and for the discussion on the physics of wetting and icing of solid surfaces.

My appreciation also goes to all the members of the Process Simulation research group at the Institute of Production Engineering and Photonic Technologies for the supportive community and inspiring discussions.

I would like to thank my family and friends for their help and support during my studies.

Contents

Abstract

Laser processing of surfaces is a powerful method for changing their properties, which can vary depending on the application. In this thesis, the wetting and icing behavior of a water droplet on laser-structured surfaces was investigated using numerical methods. A multiphase solver was extended by various surface tension models and each model was compared with analytically solvable test cases. Then, the wetting of flat surfaces was simulated in order to better investigate the interaction between the solid plate and the droplet. The wetting and icing simulations on laser-structured surfaces were performed with the model that delivered the best results in the previous tests. According to the results, the surface tension model can reproduce the modified surface characteristics due to laser processing. It was also found that both the wetting and icing behavior of the droplet depend on the simulated droplet size. During the analysis, a droplet diameter was determined at which the results no longer change. Throughout the work, the influence of numerical parameters such as interface compression and solid movement restriction was analyzed. In addition, several numerical methods were tested to obtain more stable and faster simulations.

Kurzfassung

Die Bearbeitung von Oberflächen mit Laser ist eine leistungsfähige Methode, um ihre Eigenschaften zu verändern, die je nach Anwendung unterschiedlich sein können. Im Rahmen der vorliegenden Diplomarbeit wurde das Benetzungs- und Vereisungsverhalten eines Wassertropfens auf laserstrukturierten Oberflächen mit numerischen Methoden untersucht. Ein Mehrphasensolver wurde um verschiedene Oberflächenspannungsmodelle erweitert und jedes Modell mit analytisch lösbaren Testfällen verglichen. Danach wurde die Benetzung von ebenen Oberflächen simuliert, um die Interaktion zwischen der festen Platte und dem Tropfen besser untersuchen zu können. Benetzungs- und Vereisungssimulationen auf laserstrukturierten Oberflächen wurden mit dem Modell durchgeführt, das in den vorherigen Tests die besten Ergebnisse geliefert hatte. Laut den Ergebnissen kann das Oberflächenspannungsmodell die durch die Laserbearbeitung veränderten Oberflächeneigenschaften reproduzieren. Außerdem wurde festgestellt, dass sowohl das Benetzungs- als auch das Vereisungsverhalten des Tropfens von der simulierten Tropfengröße abhängen. Während der Untersuchungen wurde ein Tropfendurchmesser ermittelt, ab dem sich die Ergebnisse nicht mehr ändern. Im Laufe der Arbeit wurde der Einfluss von numerischen Parametern wie Grenzflächenkompression und Bewegungseinschränkung von Festkörpern analysiert. Weiterhin wurden verschiedene numerische Methoden untersucht, um die Simulationen zu stabilisieren und beschleunigen.

List of Figures

List of Tables

Nomenclature

Greek symbols

α	phase volume fraction; thermal diffusivity
δ	Dirac delta function; small constant (solid movement restriction term)
κ	curvature of the interface
λ	thermal conductivity
λ_{St}	phase front parameter (Stefan problem)
μ	dynamic viscosity
ν	kinematic viscosity
ϕ	probability density function of the normal distribution; flux
ρ	density
σ	surface tension / free surface energy
σ^D	dispersive component of surface tension / free surface energy
σ^P	polar component of surface tension / free surface energy
τ	viscous stress tensor; time for formation of a full ice layer
θ	contact angle

Latin symbols

a	parameter of the normal distribution
A	liquid-gas interface area of the droplet; diagonal components of the discretization matrix of the velocity; initial liquid depth to width ratio (Marangoni flow)
A_0	initial surface area of the droplet
A_{perm}	permeability area of the mixed region
A_{SI}	steel-ice interface area
Bo	Bond number
c_α	interface compression coefficient
c_p	specific heat capacity
C	normalized capillary number (Marangoni flow)
d_b	base diameter of the droplet

D	initial liquid depth (Marangoni flow)
D_0	initial diameter of the droplet
$\boldsymbol{f}_{st}$	surface tension force
F	cumulative distribution function of the normal distribution
g	gravitational acceleration
h	height of the droplet; dimenionless stationary liquid depth (Marangoni flow)
H	energy; stationary liquid depth (Marangoni flow)
$\mathbf{H}$	non-diagonal components of the discretization matrix of the velocity
I	interface function
$\mathbf{I}$	identity matrix
k	α_S-dependent part of the solid movement restriction term
L_{fusion}	latent heat of fusion
m	slope parameter (Marangoni flow)
$\mathbf{M}$	discretization matrix of the velocity
$\hat{\boldsymbol{n}}$	unit normal vector of the interface
N	number of phases
p	pressure
r_b	base radius of the droplet
$\boldsymbol{S}_B$	gravitational force
$\boldsymbol{S}_D$	solid movement restriction term
$\boldsymbol{S}_f$	face area vector
St	Stefan number
t	time
$\hat{\boldsymbol{t}}$	unit tangential vector of the interface
T	temperature
$\mathbf{T}$	surface tension tensor
$\boldsymbol{u}$	velocity field
V_0	volume of the droplet

w	width of the droplet
W	liquid width (Marangoni flow)
x	dimenionless position (Marangoni flow); position (Stefan problem)
X	pase front position (Stefan problem)

Subscripts

$\parallel$	parallel component
$\perp$	normal component
C	cold
$curv$	curvature
f	face value
G	gas phase
H	hot
I	ice
i, j	indices of the phases
L	liquid phase
M	melting
Mar	Marangoni
r	relative; reference
S	solid phase; steel
trl	triple line
W	water

Labels

T	tensor-based model
T_d	decomposed tensor-based model
V1	vector-based model
V2	modified vector-based model
V_d	decomposed vector-based model

1 Introduction

The shape and surface area of a liquid droplet greatly influence the heat and mass transfer in a system. Since surface tension is one of the most relevant factors in determining the shape of liquids, it is important to carefully model it in multiphase simulations.

Surface tension plays a key role in bubble and droplet formation, and therefore also in wetting of solid surfaces. A component with a hydrophobic/icephobic surface is often advantageous if it is in contact with water. One example is the rotor blades of wind turbines, on which water droplets can attach and freeze. The modified profile and the increase in mass reduce the efficiency of the wind turbine. In addition, the detachment of the adhering ice means a safety risk for the surroundings. The aim of surface structuring can be to completely prevent ice adhesion or to reduce the force required to shear off the attached ice. In this case, the ice can be removed from the surface by gravity, centrifugal forces and active de-icing methods such as heating the rotor blades.

Furthermore, surface tension is essential in all applications with a free-surface liquid phase, with a mixture of several liquid phases, and with phase changes. Welding processes are good examples of the importance of surface tension. The heat released by the source melts the solid phase and a liquid pool forms, which then evaporates. During a welding process, all three force components discussed in this work occur, which are related to surface tension. The forces due to curvature act on the curved liquid surface and form the melt pool. The Marangoni forces result from the large temperature gradients at the liquid-gas interface. Since there are at least three phases, the triple line forces are essential for modeling the correct contact angles.

In the present work, interactions between water droplets and laser-structured surfaces are investigated numerically. One possibility is to simulate the wetting using only two phases (water and air). In this case, the solid surface is not modeled directly and is represented by a contact angle boundary condition [1]. The method works and enables the analysis of surfaces with different wetting conditions. However, the contact angle is a user-defined parameter and not a result of the surface tension force balance. Additionally, excluding the surface from the simulations also means that the local interactions between the droplet and the surface cannot be observed. Therefore, it is important to include the laser-structured surface in the simulations and to obtain contact angles using surface tension values from the literature.

The investigations of the present work are based on the master's thesis by Skrna [2]. Skrna examined the wetting behavior of liquids on laser-structured surfaces. Although the experiments showed hydrophobic wetting, the simulations predicted a contact angle of around 90°. In addition, Skrna's simulations were computationally expensive. Therefore the volume of the droplet was reduced compared to that used in the experiments. The aim of the present work is to analyze and improve the numerical treatment of surface tension to get closer to the experimental results. Furthermore, phase changes are also included in the simulations to model icing on laser-structured surfaces.

The biggest challenge in simulating such a phenomenon is the different scales of the water droplet and the structures of the surface. Between the droplet diameter and the surface structures used in the experiments referred to in this work, there is a factor of around 27. This means that the resolution of the surface structures at least one droplet diameter wide requires high computational costs. In addition, the complexity of surface tension modeling depends on the number of phases in the system. For two phases, the surface tension force is always well defined by the one interface between the phases, and the modeling is usually straightforward. Simulations with three or more phases get more difficult, because regions where several phases meet need particular consideration.

The thesis consist of two main parts: the theoretical background and the evaluation of the simulation results. The first part starts with an introduction to the underlying principles of surface tension and wetting of solid surfaces (Chapters 2 and 3). In Chapter 4, the governing equations and the numerical methods of solving them are presented, then the numerical formulation of the surface tension force is introduced. In Chapter 5, it is shown how the surface tension force can be included in the solver algorithm. In the second part of the thesis (Chapter 6), the simulation results are discussed. First, the freezing of water and the developed surface tension force models are compared to analytically solvable test cases (Sections 6.2 and 6.3). Afterwards, wetting on flat and laser-structured surfaces is simulated (Sections 6.4 and 6.5). Finally, the most complex simulations, icing phenomena on laser-structured surfaces are presented (Section 6.6).

2 Surface Tension

In this chapter, the phenomenon of surface tension is explained from a molecular point of view based on the work by Rapp [3].

2.1 Intermolecular Forces

In a material, the molecules are surrounded by other ones which attract the actual molecule due to chemical bonds. These cohesive forces are evenly distributed around the molecule and hold the material together. That means that the intermolecular forces are balanced, and the resulting net force is zero if the molecule is in the bulk of the material. However, surface molecules have neighbors only on the inner side (see Figure 2.1). Therefore, a net force pointing inward is observed acting on the surface molecules. In liquids, this force leads to the deformation of the surface.

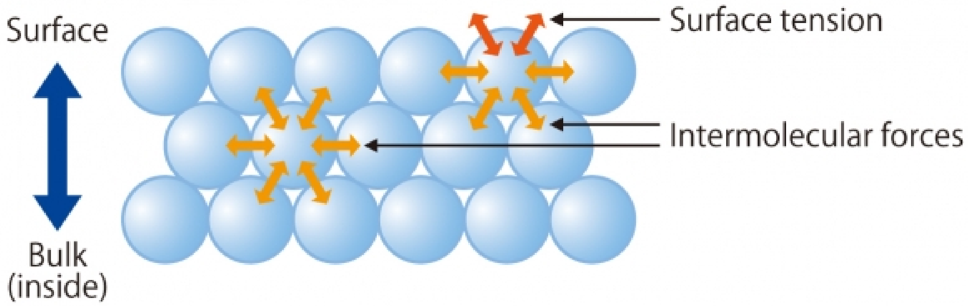

Figure 2.1: Schematic illustration of imbalanced intermolecular forces at the surface [4].

Increasing the surface area needs energy because of moving molecules from the volume to the surface. Thus, having less surface molecules with unbalanced cohesive forces is a thermodynamically more stable state with lower energy. That is why each system strives to minimize its surface area. In case of liquids, this results in a change in shape.

2.2 Free Surface Energy

The term free surface energy stands for the energy that is required to create surface area in a system. Its unit is Jm^{-2} which also explains the definition. This property depends on the surrounding material. If the other material can replace the missing chemical bonds, the intermolecular forces are more balanced, and the net force is also smaller. For that reason, the free surface energy of a material is expressed in relation to a reference material that surrounds the actual material. It is practical to take air as the reference material, as it is the case very often.

Since free surface energy is the result of the missing cohesive forces of the neighboring molecules, it is higher for a material with strong bonds. On the one hand, metals have high free surface energies, because they are held together by strong primary bonds. On the other hand, polymers have lower free surface energies, since they are characterized by weaker secondary bonds.

In the literature, the expression "free surface energy" refers to solid materials. While for liquids, the term "surface tension" is used with the unit Nm^{-1}. It is important to emphasize, that the two quantities describe the same physical phenomenon and have the same unit.

3 Wetting and Contact Angle

If a fluid interacts with a solid, forces are acting between the surface molecules of the two phases. These molecules find candidates on the surface of the other phase that take the place of their missing neighboring molecules. Depending on the free surface energy of the solid and the surface tension of the fluid, various behaviors of the fluid can be observed on the surface. This phenomenon is called the wetting behavior of the liquid. On the one hand, if it is energetically unfavorable to spread on the surface, the fluid aims to form a sphere, just like it does if it is not in contact with a surface. On the other hand, if it is energetically favorable to interact with the solid, the fluid spreads all over the surface. It can be observed that the fluid yields to minimize its surface area if an energetically more favorable scenario is available.

3.1 Young's Equation

When the liquid interacts with the solid in a surrounding fluid (usually a gas), the three phases form a triple line where they meet. The angle between the liquid and the solid is referred to as the contact angle, as shown in Figure 3.1.

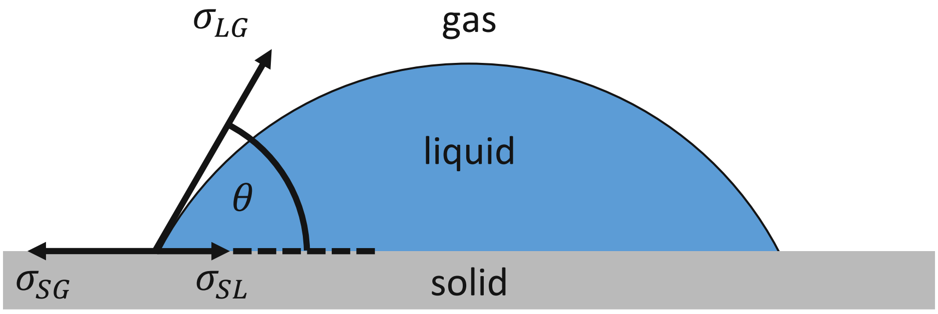

Figure 3.1: Contact angle θ and free surface energies σ_{ij} between the phases i and j at the triple line in case of a liquid droplet on a solid surface.

The contact angle θ in a system of three phases is described by Young's equation:

$$\cos\theta = \frac{\sigma_{SG} - \sigma_{SL}}{\sigma_{LG}} , \tag{3.1}$$

where σ_{SG} is the free surface energy of the solid with respect to the gas phase. Similarly, σ_{LG} stands for the surface tension of the liquid with respect to the gas phase. Finally, σ_{SL} denotes the free surface energy between solid and liquid. In general, σ_{SL} can be expressed as a function of σ_{SG} and σ_{LG}. The calculation of σ_{SL} depends on the materials and their cohesive forces at the interface. In the present work, two methods for determining σ_{SL} are discussed. First, if only dispersion forces interact at the interface, and second, if both dispersion and polar forces occur.

3.1.1 Only Dispersion Forces

Dispersion forces arise due to the attraction between fluctuating dipoles. These kinds of interactions are present between all types of molecules and atoms. The assumption that intermolecular forces are only dispersion forces applies to most metals [2]. Therefore, it is convenient to use this for modeling liquid metal, e.g. in a welding process. In this case, σ_{SL} is calculated as follows [5–7]:

$$\sigma_{SL} = \sigma_{SG} + \sigma_{LG} - 2\sqrt{\sigma_{SG}\sigma_{LG}} \; . \tag{3.2}$$

The two equations combined lead to

$$\begin{aligned} \cos\theta &= \frac{\sigma_{SG} - \sigma_{SG} - \sigma_{LG} + 2\sqrt{\sigma_{SG}\sigma_{LG}}}{\sigma_{LG}} \\ &= \frac{-\sigma_{LG} + 2\sqrt{\sigma_{SG}\sigma_{LG}}}{\sigma_{LG}} \\ &= -1 + 2\frac{\sqrt{\sigma_{SG}\sigma_{LG}}}{\sigma_{LG}} \\ &= -1 + 2\sqrt{\frac{\sigma_{SG}}{\sigma_{LG}}} \; . \end{aligned} \tag{3.3}$$

Depending on the ratio σ_{SG} to σ_{LG}, different contact angles can be observed, which can be assigned to two main wetting conditions. For contact angles $0° \leq \theta < 90°$, the liquid wets the surface. In case of water, the surface is then called hydrophilic. For contact angles $90° < \theta \leq 180°$, the liquid does not wet the surface. In case of water, the surface is then called hydrophobic. Figure 3.2 illustrates the possible wetting scenarios.

In general, hydrophilic surfaces have higher free surface energies, while hydrophobic surfaces have lower free surface energies. For a given surface, a liquid with lower surface tension makes the surface more wettable, while a liquid with higher surface tension results in a less wettable surface. If the free surface energy of the solid is equal to the surface tension of the liquid, complete wetting takes place. In contrast, if the free surface energy of the solid is close to zero, no wetting occurs.

Table 3.1: Effect of the ratio σ_{SG} to σ_{LG} on the wetting behavior of the liquid.

σ_{SG} to σ_{LG}	contact angle	wetting behavior
$\frac{1}{4} < \frac{\sigma_{SG}}{\sigma_{LG}} \leq 1$	$0° \leq \theta < 90°$	hydrophilic
$0 \leq \frac{\sigma_{SG}}{\sigma_{LG}} < \frac{1}{4}$	$90° < \theta \leq 180°$	hydrophobic

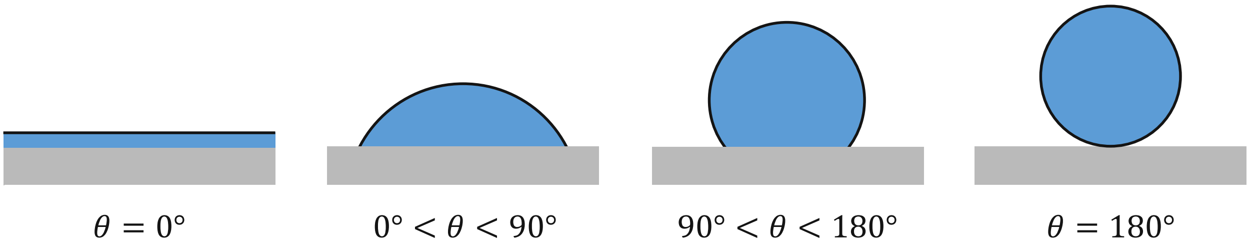

Figure 3.2: Different contact angles and corresponding wetting behaviors of a liquid droplet on a solid surface. From left to right: superhydrophilic, hydrophilic, hydrophobic, and superhydrophobic.

Equation 3.3 is useful for modeling a case with a certain contact angle without any physical meaning. σ_{SG} and σ_{LG} can be varied to obtain the preferred contact angle. This way, all kinds of wetting conditions can be investigated to validate surface tension models.

3.1.2 Dispersion and Polar Forces

Generally, intermolecular forces also consist of hydrogen bonds, dipole interactions, and metallic bonds in addition to dispersion forces (superscript D) [6]. Owens, Wendt, Rabel und Kaelble (OWRK) considered all these forces as polar forces and extended the free surface energy of solids and the surface tension of liquids by the polar component (superscript P) [2, 7]:

$$\sigma_{SG} = \sigma_{SG}^{D} + \sigma_{SG}^{P} \,, \tag{3.4}$$

$$\sigma_{LG} = \sigma_{LG}^{D} + \sigma_{LG}^{P} \,. \tag{3.5}$$

According to the OWRK method, when calculating σ_{SL}, the geometric mean of the polar components is also subtracted from the sum of σ_{SG} and σ_{LG}, analogously to the dispersion components:

$$\sigma_{SL} = \sigma_{SG} + \sigma_{LG} - 2\sqrt{\sigma_{SG}^{D}\sigma_{LG}^{D}} - 2\sqrt{\sigma_{SG}^{P}\sigma_{LG}^{P}} \,. \tag{3.6}$$

If the ratio $\sigma_{SG}^{D}/\sigma_{SG}^{P}$ is equal to the ratio $\sigma_{LG}^{D}/\sigma_{LG}^{P}$, the resulting contact angle and wetting condition correspond to those listed in Table 3.1. In contrast to the method with only dispersion forces, the OWRK method enables σ_{SG} values larger than σ_{LG}. However, it is only possible if solid and liquid are of different character (dispersive, polar). This is exactly the case at the ice-water interaction. In ice, dispersion forces are dominant, while water is of polar character, as discussed later in Section 6.6.

3.2 Analytical Solution for Small Bond Numbers

An analytical solution describing the wetting phenomenon exists, which returns the base diameter, the height and the liquid-gas interface area of the droplet as a function of the contact angle [8]. The derivation requires two main assumptions:

- The solid surface needs to be flat
- The effect of gravity is insignificant and therefore negligible

The first assumption is important, because the effect of viscous dissipation on rough surfaces is difficult to include in an analytical solution. The second assumption enables the droplet shape to be a spherical cap. The effect of gravity can be neglected for droplets with small Bond numbers, which reads

$$\mathrm{Bo} = \frac{\rho g D_0^2}{\sigma_{LG}} \ll 1 \, , \tag{3.7}$$

where ρ, g, D_0, and σ_{LG} denote density of the liquid, gravitational acceleration, initial droplet diameter, and surface tension of the liquid with respect to gas, respectively. The Bond number (named after the English physicist Wilfrid Noel Bond), also called the Eötvös number (named after the Hungarian physicist Loránd Eötvös), indicates the ratio between volume forces and surface tension forces. A small Bond number means that surface tension has the dominant role and the shape of the droplet can be assumed to be spherical. In this case, the nondimensional parameters of the droplet read [8]

$$d_b(\theta) = \frac{2\sin\theta}{[(1-\cos\theta)^2(4+2\cos\theta)]^{1/3}} \, , \tag{3.8}$$

$$h(d_b) = \left(\sqrt[3]{\frac{1}{2} + \frac{d_b^6}{64} + \sqrt{\frac{1}{4} + \frac{d_b^6}{64}}} + \sqrt[3]{\frac{1}{2} + \frac{d_b^6}{64} - \sqrt{\frac{1}{4} + \frac{d_b^6}{64}}} - \frac{d_b^2}{2} \right)^{1/2} \, , \tag{3.9}$$

$$A(d_b) = \sqrt[3]{\frac{1}{2} + \frac{d_b^6}{64} + \sqrt{\frac{1}{4} + \frac{d_b^6}{64}}} + \sqrt[3]{\frac{1}{2} + \frac{d_b^6}{64} - \sqrt{\frac{1}{4} + \frac{d_b^6}{64}}} - \frac{d_b^2}{4} \, , \tag{3.10}$$

where θ, d_b, h, and A denote contact angle, base diameter, height, and liquid-gas interface area of the droplet, respectively. d and h have been nondimensionalized by the initial diameter D_0, while A by the initial sphere area πD_0^2.

Figure 3.3 shows the functions $r_b = d_b/2$ and h over θ. The base radius r_b is zero for no wetting ($\theta = 180°$) and tends to infinity for complete wetting ($\theta = 0°$). The droplet height h is 1 for no wetting ($\theta = 180°$), which means the droplet retains its original spherical shape with diameter D_0. h vanishes for complete wetting ($\theta = 0°$) which corresponds to intuitive expectations. The two functions have an intersection point at $\theta = 90°$ with a value of $\sqrt[3]{2}/2 \approx 0.63$. This means that the droplet becomes a hemisphere for $\theta = 90°$, while the volume remains the same, therefore the diameter of the hemisphere is larger than the initial diameter D_0.

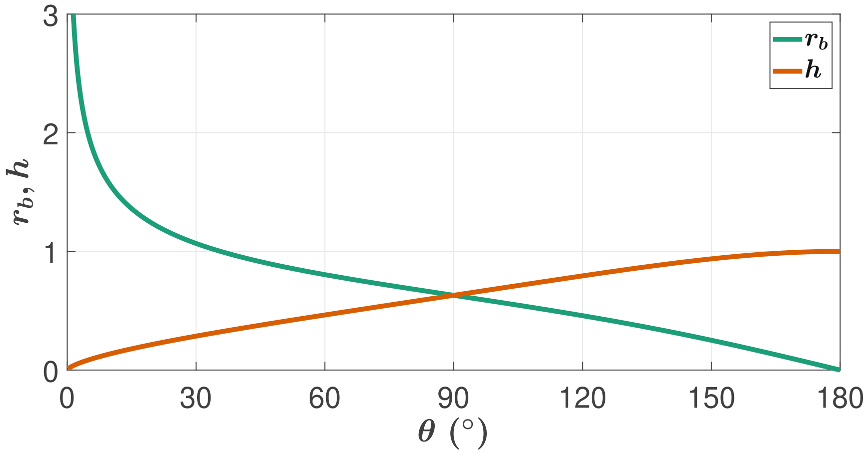

Figure 3.3: Nondimensional base radius r_b and height h of the droplet over contact angle θ, according to Equations 3.8 and 3.9.

Figure 3.4 shows the function A over θ. As expected, the liquid-gas interface area is 1 for no wetting ($\theta = 180°$) and goes to infinity for complete wetting ($\theta = 0°$). The function has a minimum at $\theta = 90°$ with a value of $2^{2/3}/2 \approx 0.79$, which corresponds to the liquid-gas interface area in the case of the hemisphere.

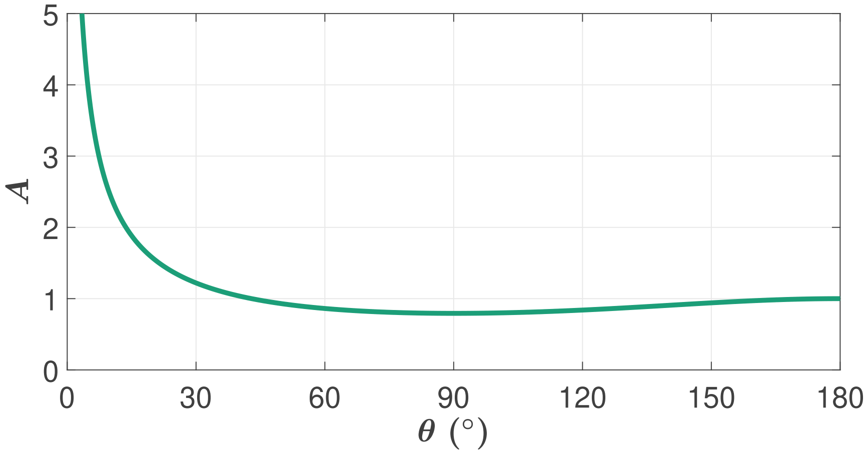

Figure 3.4: Nondimensional liquid-gas interface area A of the droplet over contact angle θ, according to Equation 3.10.

The analytical solution for small Bond numbers is useful for evaluating experimental and simulation results. If the assumption $\mathrm{Bo} \ll 1$ applies, the contact angle can be determined from the width and height of the droplet. This method is more accurate and more convenient than fitting tangential lines to the liquid-gas interface at the triple line.

4 Mathematical Modeling

The simulation of wetting including the solid surface requires a multiphase flow model. In order to reproduce real physical phenomena, it is necessary to use multiphase models in simulations of many engineering processes. In general, multiphase flow is the simultaneous flow of two or more phases. However, in numerical fluid dynamics, the expression is used for three or more phases. The reason for this is that three or more phases need a different computing technique to solve the governing equations. In this work, a mixture model is applied, where the equations are solved for a mixture of N phases. In the mixture model, the material properties are averaged according to the local phase distribution, while the velocity, pressure, and temperature fields are the same for all phases.

In Section 4.2, the governing equations are presented, which in general cannot be solved analytically. Therefore, a numerical approach, the Finite Volume Method (FVM) is used to solve these partial differential equations. In this chapter, the concept of FVM is introduced, and the mathematical formulation of surface tension is explained in detail.

4.1 Numerical Methods

In fluid dynamics, partial differential equations can be solved using many numerical methods. They all have their advantages compared to the others. In most cases, the actual physical problem determines whether a method is accurate, stable, and fast enough.

One of these methods is the Finite Volume Method, which is based on the idea of control volumes. The domain, where the physical problem is investigated, is divided into a mesh with a finite number of control volumes, also called cells. A cell is a region in space with a surface through which the fluid can flow. By solving the equations in the cells and ensuring the exchange of information between them, the conservation of mass, momentum, and energy is fulfilled. The surfaces between the cells are called faces, which are also essential for solving the equations.

After the mesh exists, the partial differential equations are integrated over each cell to obtain algebraic equations. At this point, it is practical to transform volume integrals into surface integrals with the divergence theorem of Gauss. As an example, for the volume integral of the divergence of the velocity field, it reads

$$\int_V \nabla \cdot \boldsymbol{u} \, dV = \int_S \boldsymbol{u} \cdot \boldsymbol{n} \, dS \, , \tag{4.1}$$

where $\boldsymbol{u}$ and $\boldsymbol{n}$ denote velocity field and the unit vector pointing outwards to the surface

S that encloses the volume V. Since cells consist of a finite number of faces, the surface integral is represented by a sum of face values. As a consequence for the example, the volume integral of the velocity divergence over a cell can be calculated as the sum of the fluxes through the faces. After the algebraic equations are created, they are linearized and solved iteratively. A detailed description of the FVM is provided here [9].

The simulations were performed using OpenFOAM [10], an open-source software based on the Finite Volume Method to solve mainly fluid dynamical problems. OpenFOAM consists of several built-in solvers, each of which is suitable for solving a certain problem. However, one of the biggest advantages of OpenFOAM is that the user has access to the source code. Therefore, the user can implement new models or even create new solvers.

4.2 Governing Equations

The continuity equation governing mass conservation for each phase reads

$$\frac{\partial \rho_i}{\partial t} + \nabla \cdot (\rho_i \boldsymbol{u}) = \dot{\rho}_{i,s} \ , \tag{4.2}$$

where $\boldsymbol{u}$ and ρ_i denote velocity of the mixture and partial density of phase i, respectively. Among other phenomena, freezing of water is also investigated in this work. For that reason, the source $\dot{\rho}_{i,s}$ is introduced on the right hand side, which stands for the change in ρ_i due to solidification. If the phase is not involved in phase change, the term is omitted.

The Navier-Stokes equation governing momentum conservation for the mixture of phases reads

$$\frac{\partial (\rho \boldsymbol{u})}{\partial t} + \nabla \cdot (\rho \boldsymbol{u}\boldsymbol{u}) = -\nabla p + \nabla \cdot \tau - \boldsymbol{S}_B + \boldsymbol{S}_D + \boldsymbol{f}_{st} \ , \tag{4.3}$$

where p, ρ, and τ denote pressure, density, and viscous stress tensor of the mixture, respectively. The sources $\boldsymbol{S}_B$, $\boldsymbol{S}_D$, and $\boldsymbol{f}_{st}$ stand for gravitational force, solid movement restriction term, and surface tension force, respectively. $\boldsymbol{S}_B$ and $\boldsymbol{S}_D$ are discussed directly, while the modeling of the surface tension force $\boldsymbol{f}_{st}$ is explained in the following sections.

The gravitational force $\boldsymbol{S}_B$ is modeled as

$$\boldsymbol{S}_B = g \Delta h \nabla \rho \; , \tag{4.4}$$

where g, and Δh denote the gravitational acceleration and the height difference measured from a reference height.

The solid movement restriction term $\boldsymbol{S}_D$ depends on the solid volume fraction according to the Carman-Kozeny equation [11]:

$$\boldsymbol{S}_D = -\frac{\mu}{A_{perm}} \frac{\alpha_S^2}{(1-\alpha_S)^3 + \delta} \boldsymbol{u} \; , \tag{4.5}$$

where α_S, and μ denote the solid volume fraction and the dynamic viscosity of the mixture, respectively. A_{perm} represent the permeability area of the mixed region, and δ is a small constant, so the denominator does not become zero for $\alpha_S = 1$. $\boldsymbol{S}_D$ has a small effect if the non-solid phases are dominant and holds the phases stronger for larger solid volume fractions. It is necessary because the cells involved in freezing consist of a mixture of ice, water, and air. While water and air move according to the momentum equation, ice is a solid phase that should remain where it has formed. Since the cell has one velocity for all phases, $\boldsymbol{S}_D$ ensures that both conditions are fulfilled at the same time.

Energy conservation is ensured by two equations. The convective transport of energy reads

$$\frac{\partial H_i}{\partial t} + \nabla \cdot (H_i \boldsymbol{u}) = \dot{H}_{i,s} \; , \tag{4.6}$$

where H_i denotes the energy of phase i. Similarly to the continuity equation, the change in energy due to solidification is modeled by the source $\dot{H}_{i,s}$ on the right hand side.

The conductive heat transfer is calculated as

$$\frac{\partial(\rho c_p T)}{\partial t} = \nabla \cdot (\lambda \nabla T) \; , \tag{4.7}$$

where T, c_p and λ denote temperature, specific heat capacity, and thermal conductivity of the mixture, respectively.

A detailed description of the governing equations can be found in the work by Zenz et al. [12].

4.3 Surface Tension Tensor

The following section is based on the work by Ruiz-Gutiérrez et al. [13].

In general, the stress-based surface tension tensor can be expressed as

$$\mathbf{T} = -\sigma(\mathbf{I} - \hat{\boldsymbol{n}} \otimes \hat{\boldsymbol{n}})\delta(\boldsymbol{S}(\boldsymbol{x})) \ , \tag{4.8}$$

where σ denote surface tension, $\boldsymbol{S}$ is the surface with unit normal vector $\hat{\boldsymbol{n}}$ where surface tension is active. $\delta(\boldsymbol{S}(\boldsymbol{x}))$ represents the surface density function which is the Dirac delta function for an ideal infinitely sharp interface. The term $(\mathbf{I}-\hat{\boldsymbol{n}}\otimes\hat{\boldsymbol{n}}) = \hat{\boldsymbol{t}}^{(1)}\otimes\hat{\boldsymbol{t}}^{(1)}+\hat{\boldsymbol{t}}^{(2)}\otimes\hat{\boldsymbol{t}}^{(2)}$ is a projection operator onto the tangential plane of the interface with the unitary vectors $\hat{\boldsymbol{t}}^{(1)}$ and $\hat{\boldsymbol{t}}^{(2)}$. For example, an interface normal to the x direction has $\hat{\boldsymbol{n}} = (1, 0, 0)$, therefore the x component of the tensor vanishes and only the other two components remain. Consequently, applied to a vector $\boldsymbol{a}$, the tensor term removes the component of $\boldsymbol{a}$ along $\hat{\boldsymbol{n}}$:

$$(\mathbf{I} - \hat{\boldsymbol{n}} \otimes \hat{\boldsymbol{n}})\boldsymbol{a} = \boldsymbol{a} - (\hat{\boldsymbol{n}} \cdot \boldsymbol{a})\hat{\boldsymbol{n}} \ . \tag{4.9}$$

The surface tension tensor can be decomposed into a parallel component to the interface $T_{\parallel} = \hat{\boldsymbol{t}}\cdot\mathbf{T}\cdot\hat{\boldsymbol{t}}$ and a normal component to the interface $T_{\perp} = \hat{\boldsymbol{n}}\cdot\mathbf{T}\cdot\hat{\boldsymbol{n}}$. With these components, surface tension between two phases can be defined:

$$\sigma = \int_{-\infty}^{\infty} (T_{\parallel} - T_{\perp})\, dx \ . \tag{4.10}$$

The integral formulation enables the application of the surface tension concept to smeared interfaces.

Since the surface tension tensor is determined for each interface, expression 4.8 can be converted into a formulation for each phase pair ij:

$$\mathbf{T}_{ij} = -\sigma_{ij}(\mathbf{I} - \hat{\boldsymbol{n}}_{ij} \otimes \hat{\boldsymbol{n}}_{ij})\delta_{ij}^{(S)} \ , \tag{4.11}$$

where $\hat{\boldsymbol{n}}_{ij}$ points towards phase i. The divergence of the surface tension tensor represents its spatial variation and provides the surface tension forces $\boldsymbol{f}_{st}$ acting on the interface (also proposed by Gueyffier et al. [14]). Before the divergence, the surface tension tensors of all phase pairs are summed to obtain common forces for the mixture:

$$\boldsymbol{f}_{st} = -\nabla \cdot \left(\sum_{i=1}^{N} \sum_{j=i+1}^{N} \mathbf{T}_{ij} \right) = \nabla \cdot \left[\sum_{i=1}^{N} \sum_{j=i+1}^{N} \sigma_{ij}(\mathbf{I} - \hat{\boldsymbol{n}}_{ij} \otimes \hat{\boldsymbol{n}}_{ij})\delta_{ij}^{(S)} \right] \ . \tag{4.12}$$

The surface tension force is continuous along a phase pair, but has a jump on the triple line, where the phase pairs meet. The jump is proportional to the surface tension coefficient of the phase pair, and therefore it is responsible for the realization of the contact angle. In the following, this formulation of the surface tension force is referred to as the tensor-based model.

4.4 Numerical Representation of the Dirac Delta

The Dirac delta function $\delta(x)$ is zero everywhere except at the origin, where it is infinitely large:

$$\delta(x) = \begin{cases} \infty\ , & \text{if } x = 0\ , \\ 0\ , & \text{if } x \neq 0\ . \end{cases} \tag{4.13}$$

The function $\delta(x)$ can be interpreted as the limit of the zero-centered normal distribution:

$$\delta(x) = \lim_{a\to 0} \phi(x) = \lim_{a\to 0} \frac{1}{a\sqrt{\pi}} e^{-x^2/a^2}\ . \tag{4.14}$$

The density function of the normal distribution, $\phi(x)$ (see Figure 4.2) is the derivative of the cumulative distribution function $F(x)$ (see Figure 4.1) which ranges from zero to one:

$$F(x) = \frac{1}{2}\left[1 + \operatorname{erf}\left(\frac{x}{\sqrt{a}}\right)\right]\ . \tag{4.15}$$

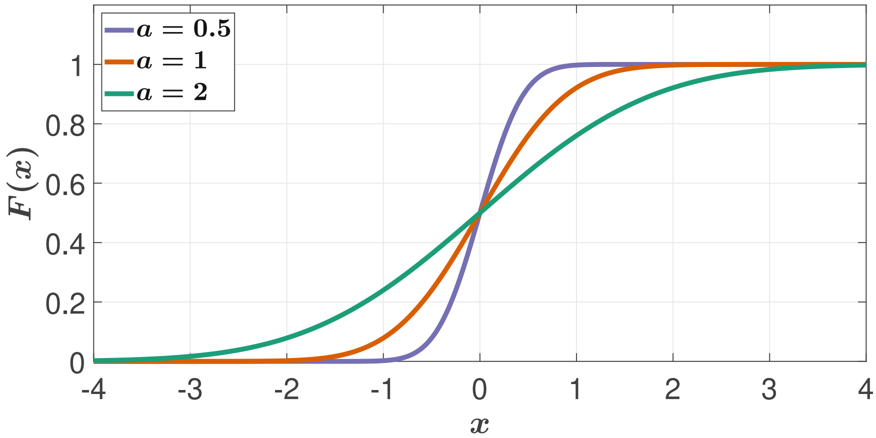

Figure 4.1: Cumulative distribution function $F(x)$ of the normal distribution with $a = 0.5$, $a = 1$, $a = 2$, according to Equation 4.15.

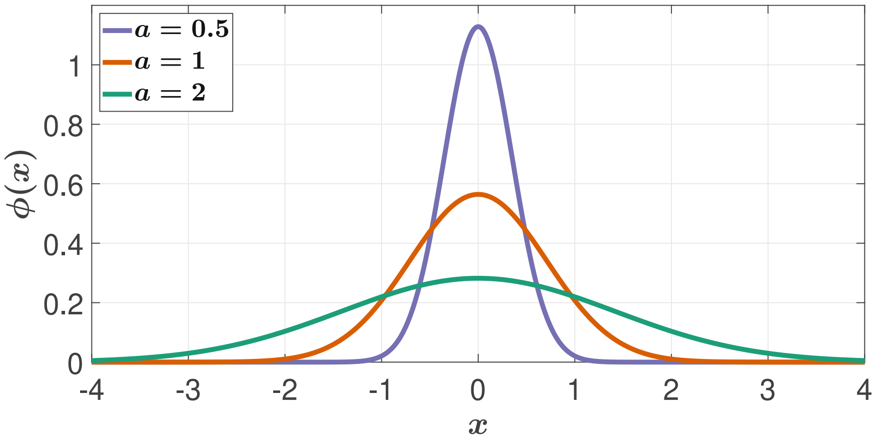

Figure 4.2: Probability density function $\phi(x)$ of the normal distribution with $a = 0.5$, $a = 1$, $a = 2$, according to Equation 4.14.

In multiphase simulations it is convenient to use the gradient of a field that takes values between zero and one over a few mesh cells. The simplest such field is the phase volume fraction α:

$$\delta_{ij}^{(S)} = |\nabla \alpha_{ij}| \ . \tag{4.16}$$

Because of the finite resolution of the domain and the inevitable numerical diffusion, the gradient of the phase volume fraction is never infinite. The surface tension force between two phases is active only on the common interface. For that reason, the phase volume fraction gradient is calculated using both gradients weighted with the opposite phase volume fraction:

$$\nabla \alpha_{ij} = \alpha_j \nabla \alpha_i - \alpha_i \nabla \alpha_j \ . \tag{4.17}$$

This way, the gradient exists only on the interface of the phase pair and points towards phase i. The unitary normal vector of the interface is defined as the normalized shared gradient introduced previously:

$$\hat{\boldsymbol{n}}_{ij} = \frac{\nabla \alpha_{ij}}{|\nabla \alpha_{ij}|} \ . \tag{4.18}$$

4.5 Vector-Based Surface Tension Model

4.5.1 Derivation of the Vector-Based Model

The derivation is based on the work by Ruiz-Gutiérrez et al. [13].

The vector-based surface tension force is derived starting from Equation 4.12:

$$\begin{aligned}
\boldsymbol{f}_{st} &= \nabla \cdot \left[\sum_{i=1}^{N} \sum_{j=i+1}^{N} \sigma_{ij} (\mathbf{I} - \hat{\boldsymbol{n}}_{ij} \otimes \hat{\boldsymbol{n}}_{ij}) |\nabla \alpha_{ij}| \right] \\
&= \sum_{i=1}^{N} \sum_{j=i+1}^{N} \nabla \cdot \left[\sigma_{ij} (\mathbf{I} - \hat{\boldsymbol{n}}_{ij} \otimes \hat{\boldsymbol{n}}_{ij}) |\nabla \alpha_{ij}| \right] \\
&= \sum_{i=1}^{N} \sum_{j=i+1}^{N} \sigma_{ij} \nabla \cdot (\mathbf{I} - \hat{\boldsymbol{n}}_{ij} \otimes \hat{\boldsymbol{n}}_{ij}) |\nabla \alpha_{ij}| + |\nabla \alpha_{ij}| (\mathbf{I} - \hat{\boldsymbol{n}}_{ij} \otimes \hat{\boldsymbol{n}}_{ij}) \nabla \sigma_{ij} \\
&= \sum_{i=1}^{N} \sum_{j=i+1}^{N} \sigma_{ij} \nabla \cdot (|\nabla \alpha_{ij}| \mathbf{I} - \hat{\boldsymbol{n}}_{ij} \otimes \nabla \alpha_{ij}) + |\nabla \alpha_{ij}| (\mathbf{I} - \hat{\boldsymbol{n}}_{ij} \otimes \hat{\boldsymbol{n}}_{ij}) \nabla \sigma_{ij} \ .
\end{aligned} \tag{4.19}$$

During the derivation, first the distributive property of the divergence operator, then the product rule for multiplication was used. For a scalar ψ and a tensor $\mathbf{A}$ this reads

$$\begin{aligned}
\nabla \cdot (\psi \mathbf{A}) &= \psi \nabla \cdot \mathbf{A} + (\nabla \psi) \cdot \mathbf{A} \\
&= \psi \nabla \cdot \mathbf{A} + \mathbf{A} \nabla \psi \ .
\end{aligned} \tag{4.20}$$

The first term on the right-hand side in Equation 4.19 can be further rewritten as follows:

$$\begin{aligned}
\nabla \cdot (|\nabla \alpha_{ij}| \mathbf{I} - \hat{\boldsymbol{n}}_{ij} \otimes \nabla \alpha_{ij}) &= \nabla \cdot (|\nabla \alpha_{ij}| \mathbf{I}) - \nabla \cdot (\hat{\boldsymbol{n}}_{ij} \otimes \nabla \alpha_{ij}) \\
&= \nabla |\nabla \alpha_{ij}| - \nabla \alpha_{ij} (\nabla \cdot \hat{\boldsymbol{n}}_{ij}) - (\hat{\boldsymbol{n}}_{ij} \cdot \nabla) \nabla \alpha_{ij} \\
&= \frac{\nabla (\nabla \alpha_{ij} \cdot \nabla \alpha_{ij})}{2 |\nabla \alpha_{ij}|} - \nabla \alpha_{ij} (\nabla \cdot \hat{\boldsymbol{n}}_{ij}) - (\hat{\boldsymbol{n}}_{ij} \cdot \nabla) \nabla \alpha_{ij} \\
&= \hat{\boldsymbol{n}}_{ij} \times (\nabla \times \nabla \alpha_{ij}) - \nabla \alpha_{ij} (\nabla \cdot \hat{\boldsymbol{n}}_{ij}) \ .
\end{aligned} \tag{4.21}$$

During the derivation the following vector calculus identities were used (for vectors $\boldsymbol{a}$, $\boldsymbol{b}$):

$$\nabla \cdot (\boldsymbol{a} \otimes \boldsymbol{b}) = \boldsymbol{b} (\nabla \cdot \boldsymbol{a}) + (\boldsymbol{a} \cdot \nabla) \boldsymbol{b} \ , \tag{4.22}$$

$$\begin{aligned}
\frac{1}{2} \nabla (\boldsymbol{a} \cdot \boldsymbol{a}) &= (\boldsymbol{a} \cdot \nabla) \boldsymbol{a} + \boldsymbol{a} \times (\nabla \times \boldsymbol{a}) \\
&= |\boldsymbol{a}| \nabla |\boldsymbol{a}| \ .
\end{aligned} \tag{4.23}$$

The last step is substituting the gradient of a phase pair in the first term on the right-hand side of Equation 4.21. With $\nabla\alpha_{ij} = \alpha_j\nabla\alpha_i - \alpha_i\nabla\alpha_j$

$$\begin{aligned}
\nabla \times \nabla\alpha_{ij} &= \nabla \times (\alpha_j\nabla\alpha_i - \alpha_i\nabla\alpha_j) \\
&= \nabla \times (\alpha_j\nabla\alpha_i) - \nabla \times (\alpha_i\nabla\alpha_j) \\
&= \alpha_j\nabla \times \nabla\alpha_i + (\nabla\alpha_j) \times (\nabla\alpha_i) - \alpha_i\nabla \times \nabla\alpha_j - (\nabla\alpha_i) \times (\nabla\alpha_j) \\
&= (\nabla\alpha_j) \times (\nabla\alpha_i) - (\nabla\alpha_i) \times (\nabla\alpha_j) \\
&= (\nabla\alpha_j) \times (\nabla\alpha_i) + (\nabla\alpha_j) \times (\nabla\alpha_i) \\
&= 2(\nabla\alpha_j) \times (\nabla\alpha_i)\ .
\end{aligned} \tag{4.24}$$

Here, the following vector calculus identities were used (for a scalar ψ, and vectors $\boldsymbol{a}$, $\boldsymbol{b}$):

$$\nabla \times (\psi\boldsymbol{a}) = \psi\nabla \times \boldsymbol{a} + (\nabla\psi) \times \boldsymbol{a}\ , \tag{4.25}$$

$$\nabla \times (\nabla\psi) = \mathbf{0}\ , \tag{4.26}$$

$$\boldsymbol{a} \times \boldsymbol{b} = -\boldsymbol{b} \times \boldsymbol{a}\ . \tag{4.27}$$

All the previous derivations and transformations summarized lead to the final expression of the vector-based surface tension model:

$$\boldsymbol{f}_{st} = \sum_{i=1}^{N}\sum_{j=i+1}^{N}\left[\underbrace{-\sigma_{ij}\kappa_{ij}\nabla\alpha_{ij}}_{\text{Curvature force}} + \underbrace{|\nabla\alpha_{ij}|(\mathbf{I} - \hat{\boldsymbol{n}}_{ij} \otimes \hat{\boldsymbol{n}}_{ij})\nabla\sigma_{ij}}_{\text{Marangoni force}} + \underbrace{2\sigma_{ij}(\nabla\alpha_i \times \nabla\alpha_j) \times \hat{\boldsymbol{n}}_{ij}}_{\text{Triple line force}}\right]\ , \tag{4.28}$$

where $\kappa_{ij} = \nabla \cdot \hat{\boldsymbol{n}}_{ij}$ is the curvature of the interface.

4.5.2 Interpretation of the Terms

Equation 4.28 consists of three different terms. These are the one due to curvature, the one considering the local variations of surface tension (Marangoni force), and the one representing the forces on the triple line, where three phases meet.

Curvature Force

$$\boldsymbol{f}_{st,curv,ij} = -\sigma_{ij}\kappa_{ij}\nabla\alpha_{ij} \tag{4.29}$$

with curvature $\kappa_{ij} = \nabla \cdot \hat{\boldsymbol{n}}_{ij}$. The first term in Equation 4.28 is responsible for the curvature of the interface and corresponds to the continuum surface force model by Brackbill et al. [15]. In two-phase models with constant surface tension σ, only this term occurs, and the surface tension force consists of exclusively this expression. Furthermore, the forces due to curvature are proportional to surface tension and the phase pair gradient. Because of the negative sign and the definition of the divergence operator, the curvature forces can point towards both phase i and j. Generally formulated, the term works against the curved interface, which means it aims to straighten the interface. Figure 4.3 shows the curvature forces on the liquid-gas interface of a liquid droplet.

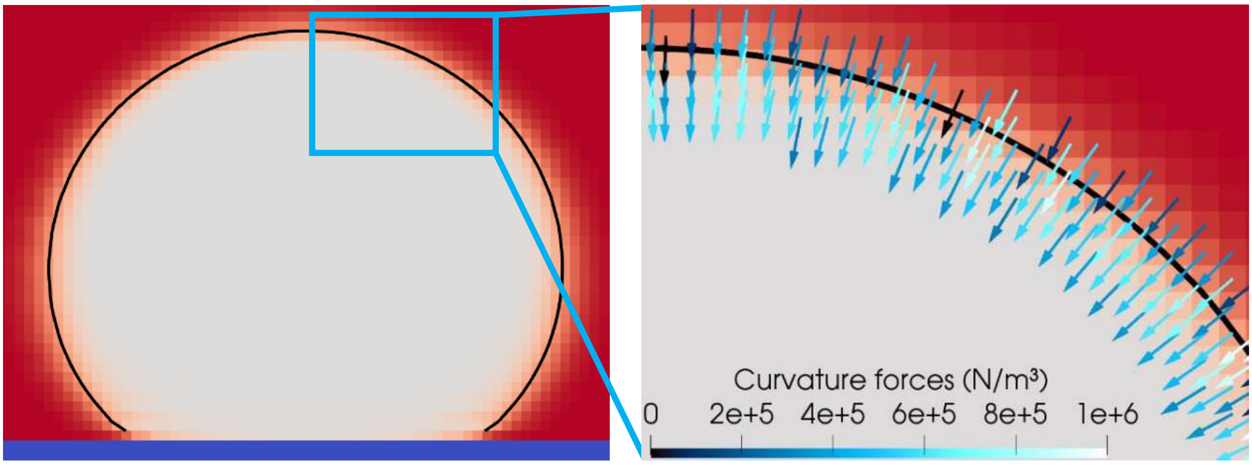

Figure 4.3: Curvature forces on the liquid-gas interface in case of a water droplet on a flat solid surface. Color blue refers to the solid surface, white to the water droplet, and red to the surrounding air. The black contour marks the liquid-gas boundary, where $\alpha_L = \alpha_G = 0.5$.

Marangoni Force

$$\boldsymbol{f}_{st,Mar,ij} = |\nabla \alpha_{ij}|(\mathbf{I} - \hat{\boldsymbol{n}}_{ij} \otimes \hat{\boldsymbol{n}}_{ij})\nabla \sigma_{ij} \tag{4.30}$$

The second term in Equation 4.28 considers the local surface tension variations which is represented by the gradient of surface tension in the formulation. In most cases, this variation is due to the temperature dependence of surface tension [16], but variations due to concentration differences in a solution also influence this term [3]. Therefore, simulations with potentially large temperature gradients should include this term.

Alternatively, the term can be also written in the form (see Equation 4.9)

$$\boldsymbol{f}_{st,Mar,ij} = |\nabla \alpha_{ij}| \left[\nabla \sigma_{ij} - \hat{\boldsymbol{n}}_{ij} \left(\nabla \sigma_{ij} \cdot \hat{\boldsymbol{n}}_{ij}\right)\right] \ . \tag{4.31}$$

Both formulations show the functionality of the Marangoni term. The first one uses the previously introduced projection tensor which takes the components of the surface tension gradient tangential to the interface. The second one computes the components of the surface tension gradients normal to the interface and subtracts them from the surface tension gradient. Although the two expressions look different, they are identical and can be derived mathematically from each other. The differentiation serves only as a guide to the interpretation.

Figure 4.4 shows the Marangoni forces due to temperature gradient. The forces are tangential to the interface and lead to deformation of the liquid surface.

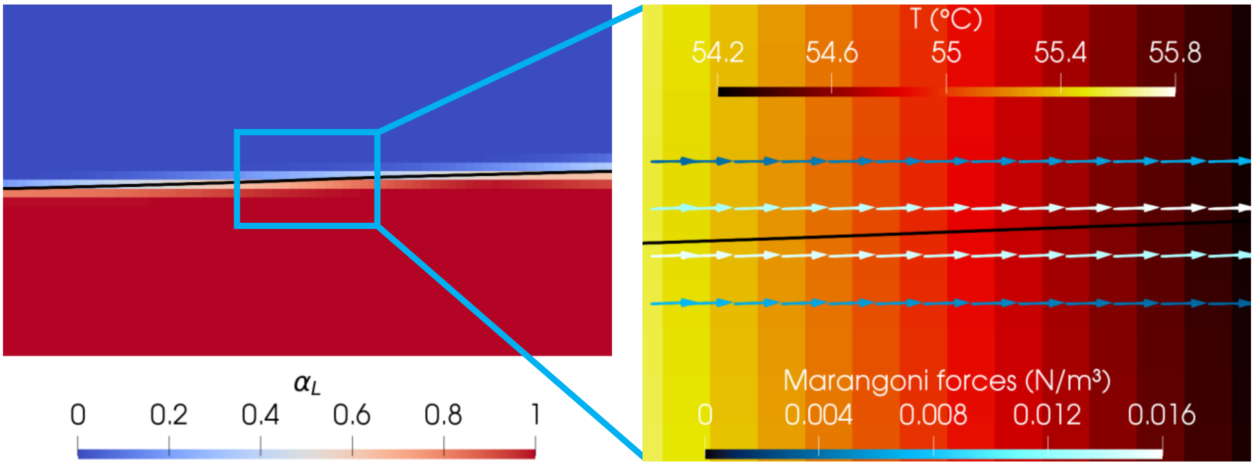

Figure 4.4: Marangoni forces in case of a two-phase flow. Marangoni forces act on the liquid-gas interface due to a linearly decreasing temperature field from left to right. The black contour marks the liquid-gas boundary, where $\alpha_L = \alpha_G = 0.5$.

An analysis of the influence of the Marangoni forces in laser material processing can be found in the paper by Zhang et al. [17].

Triple Line Force

$$\boldsymbol{f}_{st,trl,ij} = 2\sigma_{ij}(\nabla\alpha_i \times \nabla\alpha_j) \times \hat{\boldsymbol{n}}_{ij} \tag{4.32}$$

The last term in Equation 4.28 only plays a role where the gradient vectors of the two phases are not parallel to each other. Only in this case, the cross product between the two phase gradients is non-zero. This happens exactly on the triple line, where the contribution of a third phase becomes relevant. Another cross product with $\hat{\boldsymbol{n}}_{ij}$ ensures that the resulting vectors are tangential to the interface. Moreover, the term is proportional to surface tension. Therefore, the triple line forces set the correct contact angle ratios between the phases.

Figure 4.5 shows the triple line forces of a droplet wetting a hydrophobic surface. The free surface energy of a hydrophobic surface is small compared to the surface tension of the liquid, which leads to small forces on the solid-gas interface, while the forces on the liquid-gas and solid-liquid interfaces are larger.

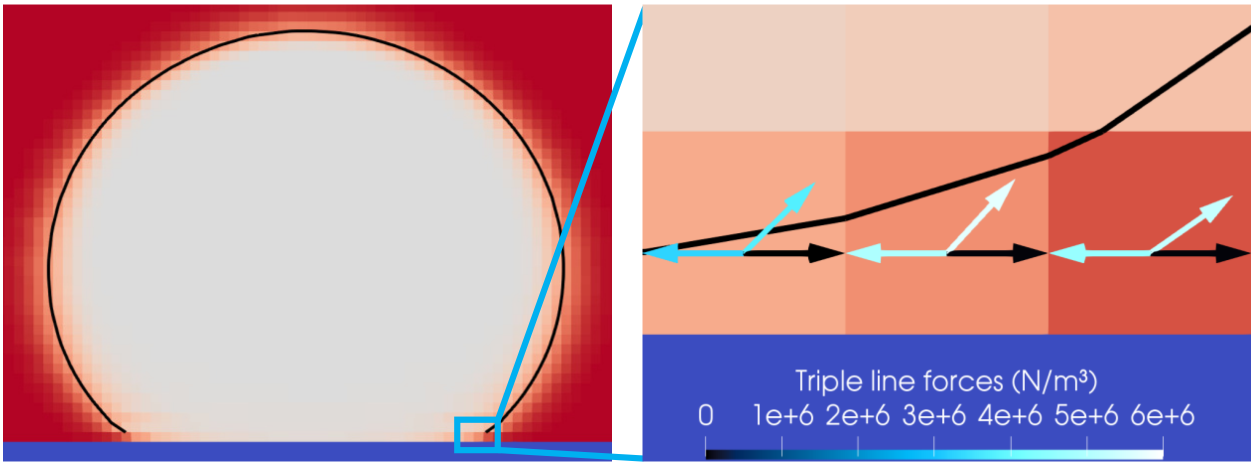

Figure 4.5: Triple line forces in case of a water droplet on a hydrophobic surface. Color blue refers to the solid surface, white to the water droplet, and red to the surrounding air. The black contour marks the liquid-gas boundary, where $\alpha_L = \alpha_G = 0.5$. $\boldsymbol{f}_{st,trl,SG}$ points to the right, $\boldsymbol{f}_{st,trl,LG}$ points diagonally upwards, $\boldsymbol{f}_{st,trl,SL}$ points to the left.

4.6 Surface Tension Decomposition

In general, the surface tension coefficient σ_{ij} is not a material parameter of one of the two phases, but a property of the interaction between two phases. The idea of surface tension decomposition is to consider surface tension forces for every phase separately, rather than for phase pairs [18, 19].

In particular, in a three-fluid system the surface tension coefficients σ_{12}, σ_{23}, σ_{13} can be transformed into the phase specific surface tension coefficients σ_1, σ_2, σ_3. In order to stay consistent with the phase-pair formulation, following decomposition relations are necessary to be satisfied:

$$\sigma_{12} = \sigma_1 + \sigma_2 \ , \tag{4.33}$$

$$\sigma_{23} = \sigma_2 + \sigma_3 \ , \tag{4.34}$$

$$\sigma_{13} = \sigma_1 + \sigma_3 \ . \tag{4.35}$$

From this system of equations, σ_1, σ_2, σ_3 can be expressed as

$$\sigma_1 = \frac{1}{2}\left(\sigma_{12} + \sigma_{13} - \sigma_{23}\right) \ , \tag{4.36}$$

$$\sigma_2 = \frac{1}{2}\left(\sigma_{12} + \sigma_{23} - \sigma_{13}\right) \ , \tag{4.37}$$

$$\sigma_3 = \frac{1}{2}\left(\sigma_{23} + \sigma_{13} - \sigma_{12}\right) \ . \tag{4.38}$$

It is important to emphasize that σ_i is not a property of phase i, because it depends on the surface tension coefficients of all three phase pairs.

With these phase specific coefficients the tensor-based surface tension model (T)

$$\boldsymbol{f}_{st}^{T} = \nabla \cdot \left[\sum_{i=1}^{N}\sum_{j=i+1}^{N} \sigma_{ij}(\mathbf{I} - \hat{\boldsymbol{n}}_{ij} \otimes \hat{\boldsymbol{n}}_{ij})|\nabla\alpha_{ij}|\right] \tag{4.39}$$

becomes

$$\boldsymbol{f}_{st}^{T_d} = \nabla \cdot \left[\sum_{i=1}^{N} \sigma_i(\mathbf{I} - \hat{\boldsymbol{n}}_i \otimes \hat{\boldsymbol{n}}_i)|\nabla\alpha_i|\right] \ , \tag{4.40}$$

while the newly introduced vector-based surface tension model (V)

$$\boldsymbol{f}_{st}^{V} = \sum_{i=1}^{N}\sum_{j=i+1}^{N} \left[-\sigma_{ij}\kappa_{ij}\nabla\alpha_{ij} + |\nabla\alpha_{ij}|(\mathbf{I} - \hat{\boldsymbol{n}}_{ij} \otimes \hat{\boldsymbol{n}}_{ij})\nabla\sigma_{ij} + 2\sigma_{ij}(\nabla\alpha_i \times \nabla\alpha_j) \times \hat{\boldsymbol{n}}_{ij}\right] \tag{4.41}$$

turns into

$$\boldsymbol{f}_{st}^{V_d} = \sum_{i=1}^{N} \left[-\sigma_i \kappa_i \nabla \alpha_i + |\nabla \alpha_i| (\mathbf{I} - \hat{\boldsymbol{n}}_i \otimes \hat{\boldsymbol{n}}_i) \nabla \sigma_i \right] \ . \tag{4.42}$$

The formulations using surface tension decomposition have the advantage that they contain the gradient of a single phase instead of the gradient between two phases. In contrast to the phase pair gradients, these single phase gradients are continuous within the domain. Therefore, the triple line force term vanishes in both expressions and the contact angles are represented by the ratio between the phase specific surface tension coefficients.

Surface tension decomposition works also for two phases. In this case, the decomposition leads to the trivial solution $\sigma_1 = \sigma_2 = \sigma_{12}/2$. Thus, there is no particular reason to introduce the method for two phases. For more than three phases, the system of equations gets overdetermined, as the number of phase pairs is larger than the number of phases [20].
In summary, the method of surface tension decomposition is beneficial, because the underlying equations get simpler. However, it can only be used to solve three-phase problems. The method can also serve to validate the general models that are valid for N phases.

5 Numerical Implementation

This chapter presents the algorithm used for solving the governing equations and describes numerical methods for including surface tension force into the solver. In addition, an important numerical parameter of multiphase flows, interface compression is also introduced.

5.1 Pressure-Velocity Coupling

As already discussed in Section 4.1, the partial differential equations that describe fluid flows are transferred into linearized algebraic equations. When solving these, the coupling of mass and momentum equations needs special treatment. In the following, one of the algorithms to manage this coupling, the so-called PISO algorithm is explained based on [21].

In fluid mechanics, to establish pressure-velocity coupling, two equations have to be solved, the Navier-Stokes equation and the continuity equation, governing momentum and mass conservation, respectively. For the sake of simplicity, the concept of the PISO algorithm is derived and presented for an incompressible fluid. A detailed description of the compressible PISO algorithm can be found in the work by Miller et al. [22]. In the incompressible case, without any sources, the governing equations have the following form:

$$\frac{\partial \boldsymbol{u}}{\partial t} + \nabla \cdot (\boldsymbol{u}\boldsymbol{u}) - \nabla \cdot (\nu \nabla \boldsymbol{u}) = -\nabla p \, , \tag{5.1}$$

$$\nabla \cdot \boldsymbol{u} = 0 \, , \tag{5.2}$$

where $\boldsymbol{u}$, p, and ν refer to velocity, pressure and kinematic viscosity. For numerical purposes, the equations are discretized and linearized, e.g. with the Finite Volume method. As the result of that, the equations become matrix equations. The momentum equation rewritten this way leads to following expression:

$$\mathbf{M}\boldsymbol{u} = -\nabla p \, , \tag{5.3}$$

$$\begin{bmatrix} * & * & & * \\ * & * & * & \\ & * & * & * \\ * & & * & * \end{bmatrix} \boldsymbol{u} = -\nabla p \, , \tag{5.4}$$

where $\mathbf{M}$ consists of all discretization coefficients of $\boldsymbol{u}$. In order to obtain velocity, multiplying both sides with $\mathbf{M}^{-1}$ is one possibility. It is often used as an initial estimate for the velocity with the pressure gradient from the last iteration step. This method is called the momentum predictor stage. However, $\mathbf{M}$ is a matrix without any exceptional properties (e.g. not diagonal).

That means, inverting $\mathbf{M}$ takes a lot of time and is computationally inefficient. Therefore, it is convenient to decompose $\mathbf{M}$ as follows:

$$\mathbf{M}\boldsymbol{u} = A\boldsymbol{u} - \mathbf{H}(\boldsymbol{u}) = -\nabla p \;, \tag{5.5}$$

$$\underbrace{\begin{bmatrix} * & * & & * \\ * & * & * & \\ & * & * & * \\ * & & * & * \end{bmatrix}}_{\mathbf{M}} \boldsymbol{u} = \underbrace{\begin{bmatrix} * & & & \\ & * & & \\ & & * & \\ & & & * \end{bmatrix}}_{A} \boldsymbol{u} + \underbrace{\begin{bmatrix} & * & & * \\ * & & * & \\ & * & & * \\ * & & * & \end{bmatrix}}_{-\mathbf{H}(\boldsymbol{u})} \boldsymbol{u} = -\nabla p \;, \tag{5.6}$$

where $A\boldsymbol{u}$ is a linear term in $\boldsymbol{u}$ with the diagonal coefficients of $\mathbf{M}$ in A. $\mathbf{H}(\boldsymbol{u})$ consists of all remaining terms and is a function of $\boldsymbol{u}$ and eventually other sources. Since $\mathbf{M}$ is known, A is also known and $\mathbf{H}(\boldsymbol{u})$ can be calculated as follows:

$$\mathbf{H}(\boldsymbol{u}) = A\boldsymbol{u} - \mathbf{M}\boldsymbol{u} \;. \tag{5.7}$$

However, the velocity field which is calculated in the momentum predictor step, and solves the momentum equation, does not satisfy the continuity equation. For that reason, the continuity equation is considered in the algorithm as follows. After multiplying Equation 5.5 by A^{-1} it reads

$$\boldsymbol{u} - A^{-1}\mathbf{H}(\boldsymbol{u}) = -A^{-1}\nabla p \;. \tag{5.8}$$

Then, taking the divergence of both sides leads to an expression that includes the continuity equation:

$$\nabla \cdot \boldsymbol{u} - \nabla \cdot (A^{-1}\mathbf{H}(\boldsymbol{u})) = -\nabla \cdot (A^{-1}\nabla p) \;. \tag{5.9}$$

Since $\nabla \cdot \boldsymbol{u} = 0$ (continuity equation), the pressure equation remains:

$$\nabla \cdot (A^{-1}\nabla p) = \nabla \cdot (A^{-1}\mathbf{H}(\boldsymbol{u})) \;. \tag{5.10}$$

The expression for the velocity (momentum corrector) is derived from Equation 5.8:

$$\boldsymbol{u} = A^{-1}\mathbf{H}(\boldsymbol{u}) - A^{-1}\nabla p \;, \tag{5.11}$$

where the pressure gradient is the result of the pressure equation. The new velocity field now satisfies the continuity equation, but not anymore the momentum equation. Hence, $\mathbf{H}(\boldsymbol{u})$ is updated using the new velocity according to Equation 5.7. After that, the pressure equation and the momentum correction are solved again. This iterative method is called the PISO algorithm. In order to achieve convergence, it is desirable to pass through the equation set at least two times per time step.

The steps of the PISO algorithm summarized:

1. Solve momentum predictor (Equation 5.3)
2. Calculate and invert A
3. Calculate $\mathbf{H}(\boldsymbol{u})$ (Equation 5.7)
4. Solve the pressure equation (Equation 5.10)
5. Correct velocity (Equation 5.11)
6. Repeat steps 3.-5. (2-3 times)
7. Go to next time step

5.2 Introducing Surface Tension Force in the Pressure-Velocity Coupling

In the previous section, the PISO algorithm without any sources was explained in detail. This section discusses the possible ways for extending the momentum equation with the surface tension force as a source term.

The incompressible momentum equation in this case reads

$$\frac{\partial \boldsymbol{u}}{\partial t} + \nabla \cdot (\boldsymbol{u}\boldsymbol{u}) - \nabla \cdot (\nu \nabla \boldsymbol{u}) = -\nabla p + \tilde{\boldsymbol{f}}_{st} \tag{5.12}$$

with the density specific surface tension $\tilde{\boldsymbol{f}}_{st} = \boldsymbol{f}_{st}/\rho$. The continuity equation remains unchanged.

5.2.1 Surface Tension Force with the Momentum Terms

The first method is where the source is written to the left-hand side of the momentum equation and is added to the terms containing velocity:

$$\mathbf{M}\boldsymbol{u} - \tilde{\boldsymbol{f}}_{st} = \begin{bmatrix} * & * & & * \\ * & * & * & \\ & * & * & * \\ * & & * & * \end{bmatrix} \boldsymbol{u} - \tilde{\boldsymbol{f}}_{st} = -\nabla p \ . \tag{5.13}$$

In contrast to the case without a source term, $\mathbf{M}\boldsymbol{u} - \tilde{\boldsymbol{f}}_{st}$ is decomposed as $A\boldsymbol{u} - \mathbf{H}(\boldsymbol{u})$, not only $\mathbf{M}\boldsymbol{u}$:

$$A\boldsymbol{u} - \mathbf{H}(\boldsymbol{u}) = \underbrace{\begin{bmatrix} * & & & \\ & * & & \\ & & * & \\ & & & * \end{bmatrix}}_{A} \boldsymbol{u} + \underbrace{\begin{bmatrix} & * & & * \\ * & & * & \\ & * & & * \\ * & & * & \end{bmatrix} \boldsymbol{u} - \tilde{\boldsymbol{f}}_{st}}_{-\mathbf{H}(\boldsymbol{u})} = -\nabla p \, . \tag{5.14}$$

Therefore, $\tilde{\boldsymbol{f}}_{st}$ is added to $\mathbf{H}(\boldsymbol{u})$ which is then calculated as follows:

$$\mathbf{H}(\boldsymbol{u}) = A\boldsymbol{u} - \mathbf{M}\boldsymbol{u} + \tilde{\boldsymbol{f}}_{st} \, . \tag{5.15}$$

All subsequent equations and calculations that depend on $\mathbf{H}(\boldsymbol{u})$ (pressure equation, momentum corrector) remain as in the case without a source term.

5.2.2 Surface Tension Force with the Pressure Gradient

In the second method, the left-hand side of the momentum equation is unaffected and $\mathbf{H}(\boldsymbol{u})$ also remains unchanged compared to the case without source term:

$$\mathbf{M}\boldsymbol{u} = A\boldsymbol{u} - \mathbf{H}(\boldsymbol{u}) = -\nabla p + \tilde{\boldsymbol{f}}_{st} \, . \tag{5.16}$$

However, the pressure equation is different, because the starting equation has an extra term. After following the same derivation way and restructuring the equation while using the distributive property of the divergence operator, the pressure equation is expressed as

$$\nabla \cdot (A^{-1}\nabla p) = \nabla \cdot (A^{-1}\mathbf{H}(\boldsymbol{u}) + A^{-1}\tilde{\boldsymbol{f}}_{st}) \, . \tag{5.17}$$

For the same reason, a term proportional to surface tension force is added to the momentum corrector as well:

$$\boldsymbol{u} = A^{-1}\mathbf{H}(\boldsymbol{u}) - A^{-1}\nabla p + A^{-1}\tilde{\boldsymbol{f}}_{st} \, . \tag{5.18}$$

Because of numerical efficiency and accuracy, OpenFOAM uses fluxes to evaluate the divergence of the fields in the pressure equation. The flux is a face field and is calculated as follows:

$$\phi = \boldsymbol{S}_f \cdot \boldsymbol{u}_f = \boldsymbol{S}_f \cdot (A^{-1}\mathbf{H}(\boldsymbol{u}))_f - \boldsymbol{S}_f \cdot A_f^{-1}\nabla p_f + \boldsymbol{S}_f \cdot A_f^{-1}\tilde{\boldsymbol{f}}_{st,f} \tag{5.19}$$

with the vector $\boldsymbol{S}_f$ normal to the face with the magnitude equal to the face area and $\boldsymbol{u}_f$ the velocity field evaluated on the faces (the subscript f refers to a face field). Consequently, if the surface tension force as a vector field is interpolated to the faces, it can be added to the pressure equation as a flux.

The term including the surface tension force can also be calculated differently. OpenFOAM provides a surface normal gradient method, which calculates the gradient of a scalar field ψ normal to the cell face as follows:

$$\nabla_\perp \psi = \boldsymbol{n}_f \cdot (\nabla \psi)_f \ , \tag{5.20}$$

where $\boldsymbol{n}_f$ is the face unit normal vector.

The surface-normal shared phase gradient calculated this way reads

$$\nabla_\perp \alpha_{ij} = \alpha_{j,f} \nabla_\perp \alpha_i - \alpha_{i,f} \nabla_\perp \alpha_j \ . \tag{5.21}$$

The surface normal gradient is a scalar field, therefore the surface tension force calculated this way is also a scalar field. Because of the structure of the surface tension force terms, this method works only for the curvature forces:

$$\tilde{f}_{st,curv,f} = -\sigma_f \kappa_f \nabla_\perp \alpha \ . \tag{5.22}$$

When using this method, the surface tension coefficient and the curvature need to be interpolated to the faces. The scalar surface tension force multiplied with the magnitude of the face area vector $|\boldsymbol{S}_f|$ can be added to the flux and the surface tension force term can be written as

$$\boldsymbol{S}_f \cdot A_f^{-1} \tilde{\boldsymbol{f}}_{st,f} = |\boldsymbol{S}_f| A_f^{-1} \tilde{f}_{st,curv,f} \ . \tag{5.23}$$

5.3 Interface Compression

The distribution and advection of phases in a velocity field is described by the following conservation equation:

$$\frac{\partial \rho_i}{\partial t} + \nabla \cdot (\rho_i \boldsymbol{u}) = \nabla \cdot (\alpha_i (1 - \alpha_i) \rho_i \boldsymbol{u}_r) \ , \tag{5.24}$$

where the relative velocity $\boldsymbol{u}_r$ is defined as

$$\boldsymbol{u}_r = -c_\alpha |\boldsymbol{u}| \frac{\nabla \alpha_i}{|\nabla \alpha_i|} \ , \tag{5.25}$$

while the term that comes from solidification is excluded for simplicity.

For numerical purposes, an artificial term on the right hand side in Equation 5.24 is introduced, which aims to maintain a sharp interface. The factor $\alpha_i(1 - \alpha_i)$ ensures that the compression is only active on the diffuse interface. Note that it is zero for an infinitely sharp interface, i.e. for a step in the volume fraction α_i. The direction of $\boldsymbol{u}_r$ is determined by the relevant phase gradient, therefore the compression acts orthogonal to the interface. The value of c_α can be adjusted by the user to control the influence of interface compression.

Interface compression is calculated individually for each phase. However, it makes only sense if the phase can move freely, i.e. on interfaces without solid. For that reason, interface compression is modified in a way that it is only applied between liquid and gas phases. Modeling of the interface compression this way reduces the unphysical artificial velocities at solid interfaces and leads to more stable and accurate results.

As shown in Figure 5.1, the effect of interface compression depends on c_α. In general, values between 0 and 1.5 work in most cases. However, for a small c_α, the solution is distorted by numerical diffusion, since the discontinuity of the phases as a discrete property is described by a continuum model. This leads to a smeared interface between the phases. In contrast, $c_\alpha > 1.5$ cause artificial velocities and the desired functionality is no longer guaranteed.

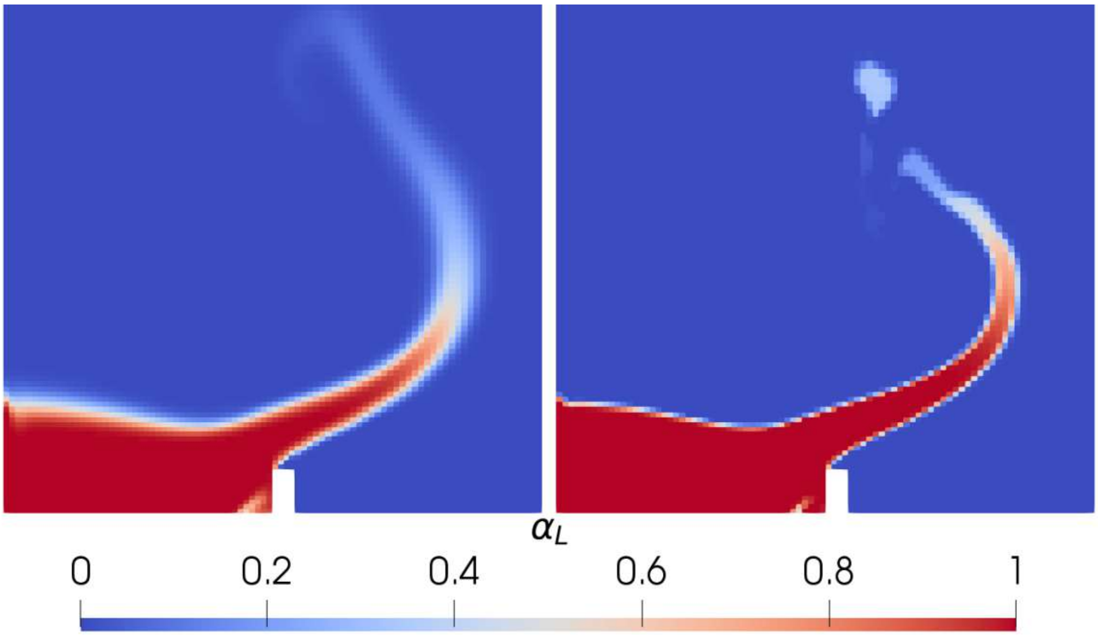

Figure 5.1: Comparison of $c_\alpha = 0$ (left) and $c_\alpha = 1$ (right) for the dam break case [23].

Another option that provides sharp interfaces is the geometric interface reconstruction (isoAdvector). However, it only works for two phases and incompressible flows. Since the models in the present work are developed for simulations of material processing, where a compressible flow of more than two phases occurs, the method mentioned above is not considered as a solution to the problem.

6 Results

In this chapter, the simulation results are evaluated. First, an overview of the different surface tension force models is provided. Afterwards, the phase change and surface tension models are verified with analytically solvable test cases. Then, wetting on flat and laser-structured surfaces is investigated, followed by simulations of icing on laser-structured surfaces.

6.1 Surface Tension Models Used in the Simulations

The simulations were carried out with four different surface tension models. These were the tensor-based model (T), the decomposed tensor-based model ($\mathrm{T_d}$), the vector-based model (V1), and the modified vector based model (V2). The implementation of the four models and the differences between them are introduced in the following sections.

6.1.1 Tensor-Based Model (T)

As already mentioned in Section 4.3, the tensor based model can be expressed as follows:

$$\boldsymbol{f}_{st}^{T} = \nabla \cdot \left[\sum_{i=1}^{N} \sum_{j=i+1}^{N} \sigma_{ij} (\mathbf{I} - \hat{\boldsymbol{n}}_{ij} \otimes \hat{\boldsymbol{n}}_{ij}) |\nabla \alpha_{ij}| \right] . \tag{6.1}$$

The resulting vector field is added to the momentum terms, as laid out in 5.2.1.

6.1.2 Decomposed Tensor-Based Model ($\mathrm{T_d}$)

The decomposed tensor-based model is derived from the tensor-based model. Instead of phase pairs, this model is formulated for each phase. Therefore, the expression contains the phase specific surface tension coefficients and the single phase gradients according to 4.6:

$$\boldsymbol{f}_{st}^{T_d} = \nabla \cdot \left[\sum_{i=1}^{N} \sigma_i (\mathbf{I} - \hat{\boldsymbol{n}}_i \otimes \hat{\boldsymbol{n}}_i) |\nabla \alpha_i| \right] . \tag{6.2}$$

The surface tension force is applied to the momentum terms.

6.1.3 Vector-Based Model (V1)

As shown in 4.5.1, the vector-based model is derived from the tensor-based model, and reads

$$\boldsymbol{f}_{st}^V = \sum_{i=1}^{N} \sum_{j=i+1}^{N} \left[\underbrace{-\sigma_{ij}\kappa_{ij}\nabla\alpha_{ij}}_{\text{Curvature force}} + \underbrace{|\nabla\alpha_{ij}|(\mathbf{I} - \hat{\boldsymbol{n}}_{ij}\otimes\hat{\boldsymbol{n}}_{ij})\nabla\sigma_{ij}}_{\text{Marangoni force}} + \underbrace{2\sigma_{ij}(\nabla\alpha_i\times\nabla\alpha_j)\times\hat{\boldsymbol{n}}_{ij}}_{\text{Triple line force}} \right] \tag{6.3}$$

with $\kappa_{ij} = \nabla \cdot \hat{\boldsymbol{n}}_{ij}$, the curvature of the interface. Similar to the tensor-based models, the surface tension force is added to the momentum terms.

6.1.4 Modified Vector-Based Model (V2)

In the modified vector-based model, the forces due to curvature are calculated using the surface normal gradient method. Then, the curvature forces are added to the pressure gradient, and are included in the pressure-velocity coupling as a flux, according to 5.2.2. Marangoni and triple line forces are still interpreted as momentum terms.

6.2 Two-Phase Stefan Problem

Later in this work, freezing of water droplets will be investigated. To validate phase changes, especially solidification, the two-phase Stefan problem was simulated, which is described in the following.

In the one-dimensional case, a semi-infinite liquid slab is considered with a temperature above melting temperature. On the front, a temperature below melting temperature is imposed, constantly cooling the slab, as shown in Figure 6.1. The density in the frozen and liquid regions was chosen to be the same ($\rho_S = \rho_L = \rho$), so that no convection occurs in the liquid, only diffusion.

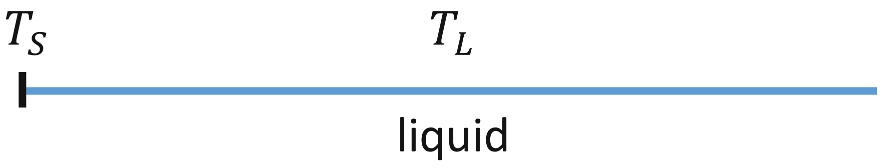

Figure 6.1: Initial conditions of the two-phase Stefan problem.

The heat conduction equation in the frozen region reads

$$\frac{\partial T}{\partial t} = \frac{\lambda_S}{\rho c_{p,S}} \frac{\partial^2 T}{\partial x^2} \,, \qquad x < X(t) \,. \tag{6.4}$$

The heat conduction equation in the liquid region reads

$$\frac{\partial T}{\partial t} = \frac{\lambda_L}{\rho c_{p,L}} \frac{\partial^2 T}{\partial x^2} \ , \quad X(t) < x \ . \tag{6.5}$$

The initial condition is the liquid temperature:

$$T(x,0) = T_L > T_M \ . \tag{6.6}$$

The boundary conditions read

$$T(0,t) = T_S < T_M \ , \tag{6.7}$$

$$\lim_{x \to \infty} T(x,t) = T_L \ . \tag{6.8}$$

The Stefan condition at the phase front connects the two regions:

$$\rho L_{fusion} \frac{dX(t)}{dt} = \lambda_S \left. \frac{\partial T}{\partial x} \right|_{X(t)^-} - \lambda_L \left. \frac{\partial T}{\partial x} \right|_{X(t)^+} \ , \tag{6.9}$$

where L_{fusion} denotes the latent heat of fusion.

6.2.1 Analytical Solution

The position of the phase front can be derived analytically [24]:

$$X(t) = 2\lambda_{St}\sqrt{\alpha_S t} \quad \text{with} \quad \alpha_S = \frac{\lambda_S}{\rho c_{p,S}} \ , \tag{6.10}$$

where α_S denotes the thermal diffusivity of the solid.

The parameter λ_{St} can be determined by solving the following equation numerically, e.g. with the Newton-Raphson method:

$$\frac{\mathrm{St}_S}{\exp({\lambda_{St}}^2)\mathrm{erf}(\lambda_{St})} - \frac{\mathrm{St}_L}{\sqrt{\frac{\alpha_S}{\alpha_L}} \exp\left({\lambda_{St}}^2 \frac{\alpha_S}{\alpha_L}\right) \mathrm{erfc}\left(\lambda_{St}\sqrt{\frac{\alpha_S}{\alpha_L}}\right)} = \lambda_{St}\sqrt{\pi} \ . \tag{6.11}$$

The parameters St_S and St_L are the Stefan numbers of the solid and the liquid, respectively:

$$\mathrm{St}_S = \frac{c_{p,S}(T_M - T_S)}{L_{fusion}} \ , \quad \mathrm{St}_L = \frac{c_{p,L}(T_L - T_M)}{L_{fusion}} \ . \tag{6.12}$$

The functions $\mathrm{erf}(x)$ and $\mathrm{erfc}(x)$ denote the error function and the complementary error function, respectively.

6.2.2 Simulation

In the simulations, a one-dimensional, 10 mm long domain was used with 800 cells. That means that the cell size was 12.5 µm.

Table 6.1 contains the material properties and temperatures used in the simulations. All material properties and temperatures correspond to those used later in the simulations with icing of laser-structured surfaces in Section 6.6.

Table 6.1: Material properties and temperatures applied in the two-phase Stefan problem.

Property	Value	Unit
Density ρ	1000	kg m^{-3}
Specific heat capacity (solid) $c_{p,S}$	2050	J kg^{-1} K^{-1}
Specific heat capacity (liquid) $c_{p,L}$	4220	J kg^{-1} K^{-1}
Thermal conductivity (solid) λ_S	2.22	W m^{-1} K^{-1}
Thermal conductivity (liquid) λ_L	0.56	W m^{-1} K^{-1}
Solid temperature T_S	-30	°C
Liquid temperature T_L	1	°C
Melting temperature T_M	0	°C
Latent heat of fusion L_{fusion}	$3.34 \cdot 10^5$	J kg^{-1}

Figure 6.2 compares the analytical solution and the simulation results. The simulation is in good agreement with the analytical solution, no noticeable differences can be identified.

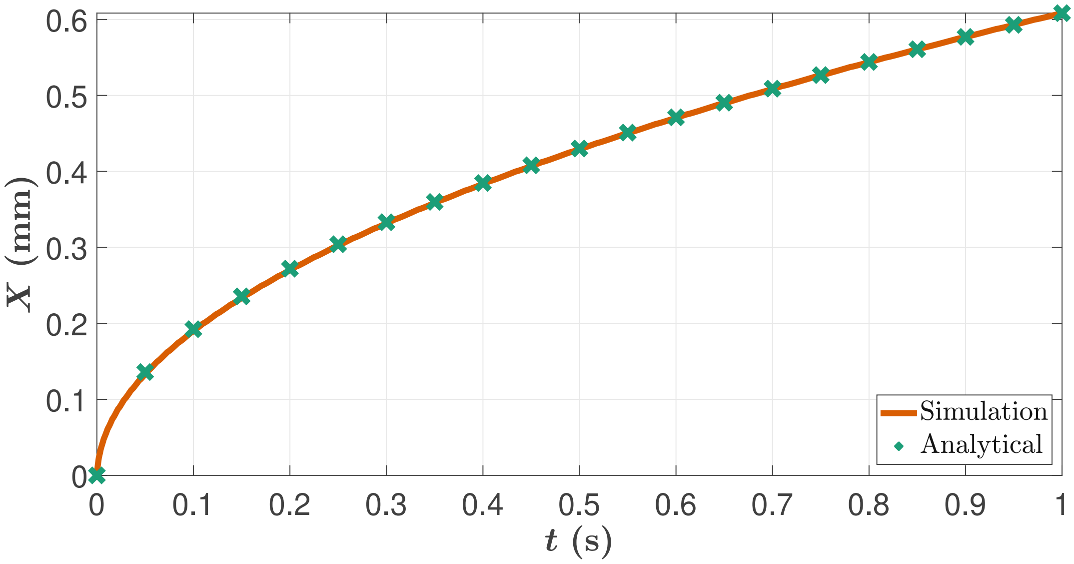

Figure 6.2: Analytical and simulated phase front positions X over time of the two-phase Stefan problem.

Plotting the absolute error (Figure 6.3) shows that the simulation underestimates the analytical solution only by a few micrometers. Knowing that the cell size was 12.5 µm, the absolute error is always smaller than one cell. The error is larger at the beginning, when the phase front moves faster and converges to zero afterward.

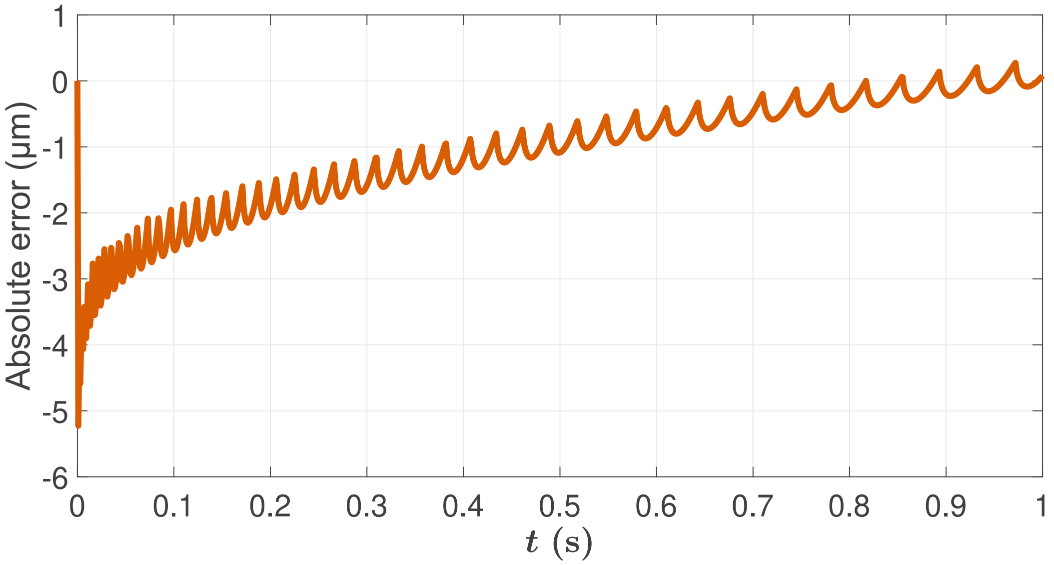

Figure 6.3: Absolute error of the simulated phase front position over time of the two-phase Stefan problem.

6.3 Two-Phase Marangoni Driven Flow

This numerical test case aims to validate the curvature and Marangoni forces using two phases. The liquid in a two-dimensional cavity is driven by Marangoni forces due to surface tension gradients. This is achieved by using a linearly decreasing temperature field from the left to the right wall. The surface tension between liquid and gas is set to decrease with increasing temperature. Therefore, Marangoni forces directed to the right act on the liquid surface. A possible initial configuration of the problem is shown in Figure 6.4 with the phase distribution and walls of different temperatures.

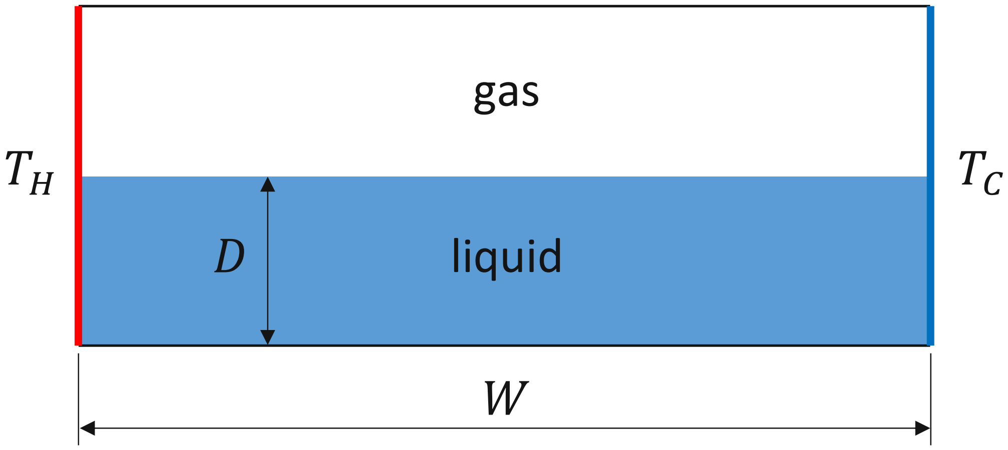

Figure 6.4: Initial phase distribution and wall temperatures of the two-phase Marangoni driven flow.

6.3.1 Analytical Solution

An analytical solution derived by Sen and Davis [25] exists which is valid for an incompressible steady-state flow without gravity. For a liquid with initial depth to width ratio $A = D/W$, the dimensionless stationary liquid depth $h = H/D$ as a function of the dimensionless position x ($x_{left} = -0.5$, $x_{right} = 0.5$) reads

$$h = 1 - \frac{AC}{16}\left[x(4x^2-3) + \frac{4}{3}m(12x^2-1)\right] + O(A^2)\ . \tag{6.13}$$

The parameter C denotes the normalized capillary number:

$$C = \frac{d\sigma}{dT}\frac{T_H - T_C}{\sigma_r A^3}\ , \tag{6.14}$$

where $d\sigma/dT$, T_H, T_C and σ_r denote derivative of surface tension at reference temperature, temperature at the hot wall, temperature at the cold wall and surface tension at reference temperature, respectively. The reference temperature is $T_r = \frac{1}{2}(T_H - T_C)$.

m is a parameter proportional to the slope of the liquid surface at the walls:

$$m = \frac{\tan(\theta - \frac{\pi}{2})}{A^2 C} \; , \tag{6.15}$$

where θ denotes contact angle. Accordingly, $m < 0$ means hydrophilic wetting, while $m > 0$ represents hydrophobic wetting. $m = 0$ corresponds to $\theta = 90°$, the transition between hydrophilic and hydrophobic wetting.

$O(A^2)$ refers to the higher order terms. If the liquid slot is shallow, A is small, and therefore the higher order terms in Equation 6.13 can be neglected. Furthermore, the derivative of h with respect to x provides more information about the behavior of the solution:

$$h' = \frac{AC}{16}\left(12x^2 - 3 + 32mx\right) \; . \tag{6.16}$$

The liquid depth h has an extremum where $h' = 0$, which results in following x_1 and x_2 values:

$$x_{1,2} = -\frac{4}{3}m \pm \frac{\sqrt{64m^2 + 9}}{6} \; . \tag{6.17}$$

For hydrophilic surfaces ($m < 0$), h has one minimum in the range $-0.5 < x < 0$. For hydrophobic surfaces ($m > 0$), h has one maximum in the range $0 < x < 0.5$. For $m = 0$, h has one minimum and one maximum at the boundaries, i.e. at $x = -0.5$ and $x = 0.5$, respectively.

6.3.2 Simulation

Table 6.2 contains the parameters used in the simulations.

Table 6.2: Parameters of the two-phase Marangoni driven flow investigated in this work.

Property	Value	Unit
Initial liquid depth D	0.2	m
Liquid width W	1	m
Aspect ratio A	0.2	-
Temperature at left wall T_H	60	°C
Temperature at left wall T_C	50	°C
Reference temperature $T_r = \frac{1}{2}(T_H - T_C)$	55	°C
Surface tension at reference temperature σ_r	0.01	$\mathrm{N\ m^{-1}}$
Surface tension derivative $\frac{d\sigma}{dT}$	$4 \cdot 10^{-5}$	$\mathrm{N\ m^{-1}\ K^{-1}}$
Normalized Capillary number C	5	-
Contact angle θ	90	°
Slope parameter m	0	-

The slope parameter m is set to zero in the simulations. In this case, the analytical solution is symmetrical and has its extrema at the boundaries.

Figure 6.5 shows the stationary solution with the temperature gradient and the velocity vectors. As expected, Marangoni forces at the liquid-gas interface drive the flow to lower temperatures. A vortex is observed with the highest velocities at the liquid surface.

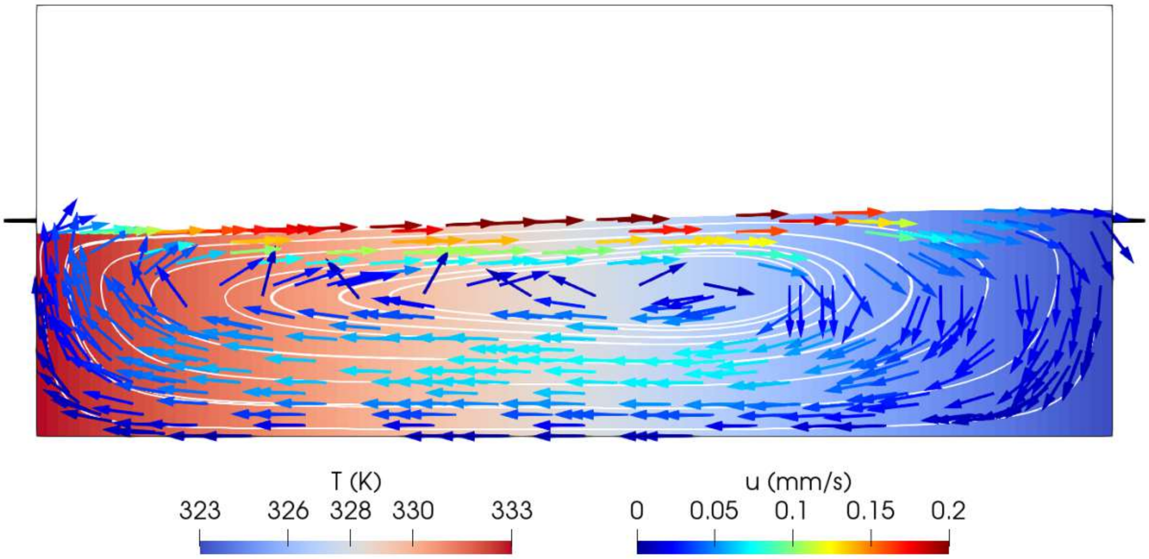

Figure 6.5: Steady-state temperature and velocity fields obtained from simulation of the two-phase Marangoni driven flow. The white lines show the streamlines in the liquid, the black lines mark the initial liquid depth.

As shown in Table 6.3, the analytical solution according to Sen and Davis without higher order terms is a deflection of 12.5 mm on both walls. The table also contains the simulations performed by Francois et al. [26] and Saldi [27], both using 100 cells in x direction, thus a cell size of $\Delta x = 10$ mm, similar to the present work.

Table 6.3: Comparison of analytical and simulated liquid depths at the hot and cold walls.

References	Depth at hot wall (mm)	Depth at cold wall (mm)
Sen and Davis, 1982 (analytical)	187.5	212.5
Francois et al., 2006 (simulation)	187	209
Saldi, 2012 (simulation)	187	208
tensor-based model T	187.57	211.69
vector-based model V1	187.92	211.54
modified vector-based model V2	188.38	211.28

All three surface tension models predict the liquid depth with great accuracy. Compared to the results of Francios et al. and Saldi, they perform well especially on the cold wall, where the liquid surface increases. The vector-based models underestimate deflection slightly more than the tensor-based model, but the relative error is less than 1% on both sides.

In order to check the influence of the cell size, the simulations were also run with $\Delta x = 5$ mm. Figure 6.6 shows the deflections on both walls for $\Delta x = 10$ mm and $\Delta x = 5$ mm. In general, all three models deliver more accurate results and the tendencies are the same as for $\Delta x = 10$ mm.

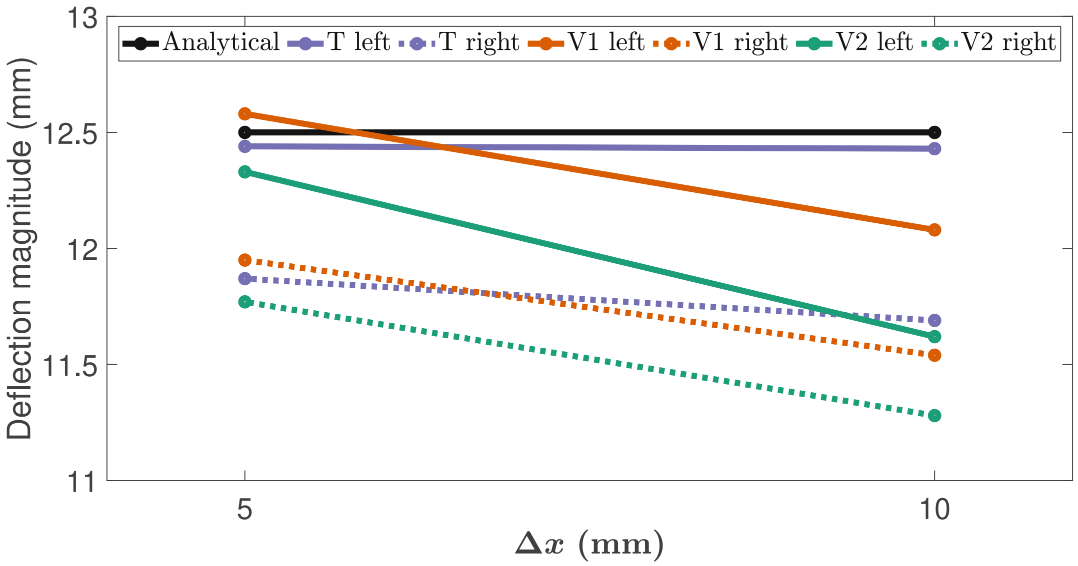

Figure 6.6: Dependence of deflection magnitude on the cell size for the three surface tension models.

6.4 Droplet on Flat Surface

The main purpose of the flat surface simulations was to test and validate curvature and triple line forces. The aim of each simulation was to reach steady state conditions, where the droplet lies still on the surface and the prescribed contact angle has established.

6.4.1 Simulation Settings

When a spherical droplet is dropped onto the surface from a certain height, the dynamic process leads to trapped air under the droplet [2]. Therefore, the starting configuration in this work was a cube with a side length of 2 mm lying on the surface, as shown in Figure 6.7. This droplet volume corresponds to that used in the experiments and enables the observation of real water droplet sizes. In the figure, color blue refers to the solid surface, white to the water droplet, and red to the surrounding air. This color code is applied for all subsequent figures.

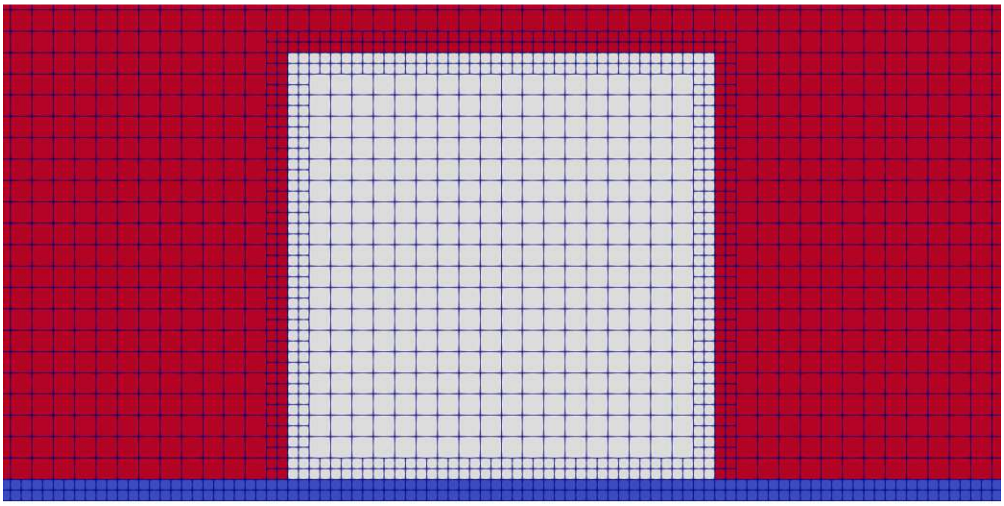

Figure 6.7: Cube-shaped initial droplet to prevent trapped air under the droplet.

The figure also contains mesh cells. To reduce the number of cells and thus the simulation time, dynamic refinement was used around the liquid phase. That means that cells with a value of α_L in a certain range were refined, e.g. between 0.1 and 0.9. This leads to a refinement only at the liquid surface, where surface tension forces act and higher mesh resolution is necessary.

The droplet material was set to be water with density of $\rho = 1000$ kg/m^3, kinematic viscosity of $\nu = 10^{-6}$ m^2/s and surface tension of $\sigma_{LG} = 0.0728$ N/m. These material properties and the corresponding droplet diameter resulted in a Bond number of Bo = 0.83. That means that the analytical solution for small Bond number is not perfectly applicable to validate the following simulations. However, since all simulations with the laser-structured surface were performed with smaller Bond numbers, the Bond number of 0.83 serves as a good comparison to see the validity range of the analytical solution.

6.4.2 Surface Tension Coefficients

To investigate different wetting conditions and contact angles, the free surface energy of the solid surface was varied. It is convenient to use the method for only dispersion forces, because the one unknown σ_{SG} can be expressed via σ_{LG} and θ (Equation 3.3):

$$\sigma_{SG} = \sigma_{LG} \frac{(\cos\theta + 1)^2}{4} \; . \tag{6.18}$$

Then, the free surface energy between solid and liquid is calculated as a function of σ_{LG} and σ_{SG} (see Equation 3.2):

$$\sigma_{SL} = \sigma_{SG} + \sigma_{LG} - 2\sqrt{\sigma_{SG}\sigma_{LG}} \; . \tag{6.19}$$

Test simulations of three different contact angles were run. Hydrophilic wetting was represented by $\theta = 30°$, hydrophobic wetting by $\theta = 150°$ and the transition between them by $\theta = 90°$. Table 6.4 shows the surface tension and free surface energy values of the three cases. According to Young's equation, for a given liquid, hydrophilic surfaces have small values of σ_{SL}, while hydrophobic surfaces have small values of σ_{SG} compared to the other two. For $\theta = 90°$, σ_{SG} equals σ_{SL} to achieve balance of the triple line forces.

Table 6.4: Surface tension and free surface energy coefficients to achieve the given contact angles.

contact angle θ (°)	σ_{LG} (N/m)	σ_{SG} (N/m)	σ_{SL} (N/m)
30	$7.28 \cdot 10^{-2}$	$6.34 \cdot 10^{-2}$	$3.27 \cdot 10^{-4}$
90	$7.28 \cdot 10^{-2}$	$1.82 \cdot 10^{-2}$	$1.82 \cdot 10^{-2}$
150	$7.28 \cdot 10^{-2}$	$3.27 \cdot 10^{-4}$	$6.34 \cdot 10^{-2}$

6.4.3 Effect of Interface Compression

Since the cube as initial shape has a contact angle of $\theta = 90°$, this contact angle was the easiest to start with. Therefore, the first attempts were performed with $\theta = 90°$. These simulations showed that the vector-based models depend on the value of c_α used for interface compression (Section 5.3). Figures 6.8 and 6.9 show the width and height of the droplet over time. It can be seen that both quantities oscillate without damping if interface compression is larger than 0.6. With $c_\alpha = 0.6$ it was possible to obtain a stationary solution that oscillates minimally compared to the dimensions of the droplet. Therefore, $c_\alpha = 0.6$ was used for the flat surface simulations. The side effect of the small interface compression value is reflected in the diffuse interface, which spans over more cells than it would with a larger value of c_α.

Note that $c_\alpha = 0.6$ is the best value for obtaining a steady-state solution, but not necessarily the physically right value. If the goal was to investigate the dynamic droplet behavior, a larger c_α might fit better with the experimental results.

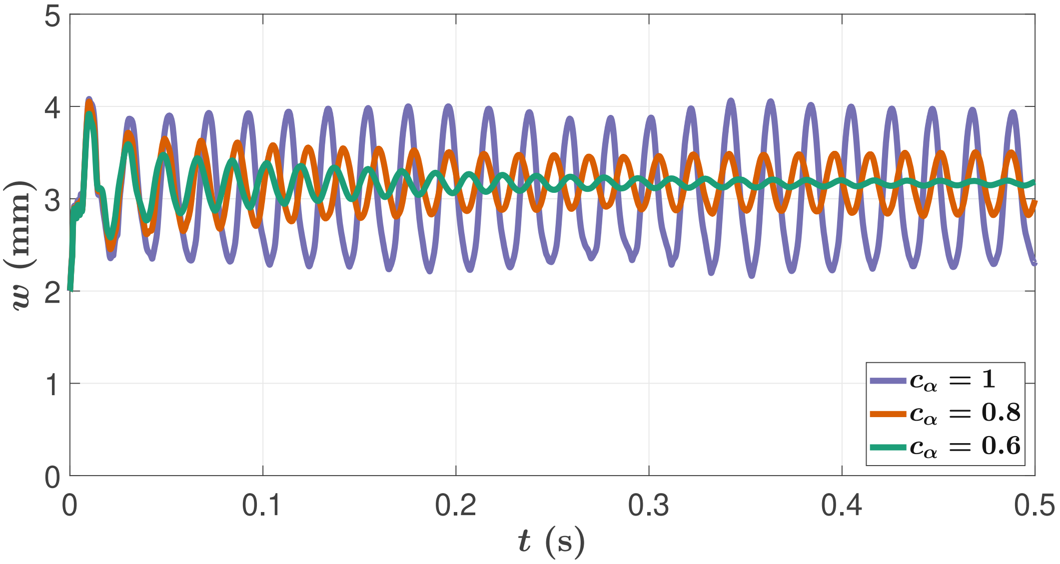

Figure 6.8: Dependence of droplet width w over time on the interface compression c_α.

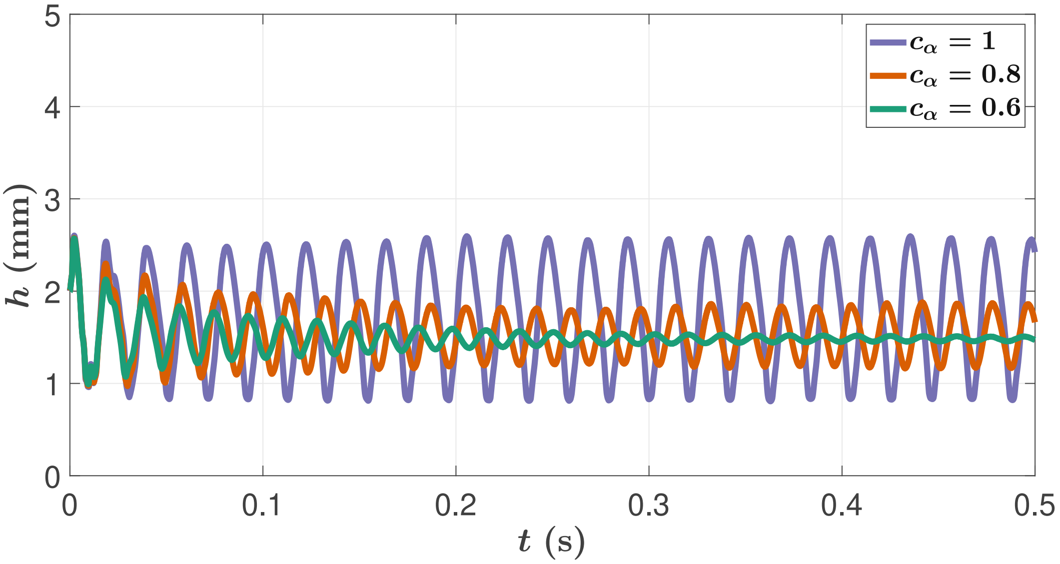

Figure 6.9: Dependence of droplet height h over time on the interface compression c_α.

6.4.4 Tensor-Based Models

First, the three simulations were run with the tensor-based model (T). Figures 6.10a, 6.10c and 6.10e (left column) show the results. In the figures, the magenta and green lines refer to the base diameter and the droplet height calculated using Equations 3.8 and 3.9. These values are valid for Bo ≪ 1. The current Bond number is 0.83, which can lead to droplets with slightly less height and more base diameter.

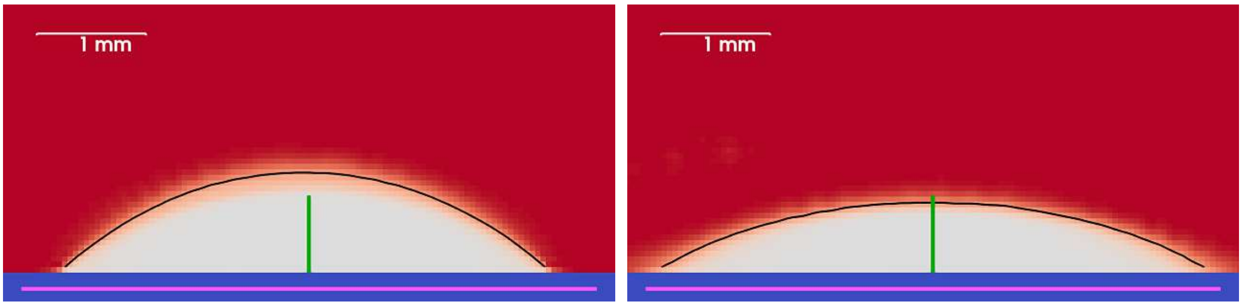

(a) $\theta = 30°$, tensor-based (T)

(b) $\theta = 30°$, decomposed tensor-based ($\mathrm{T_d}$)

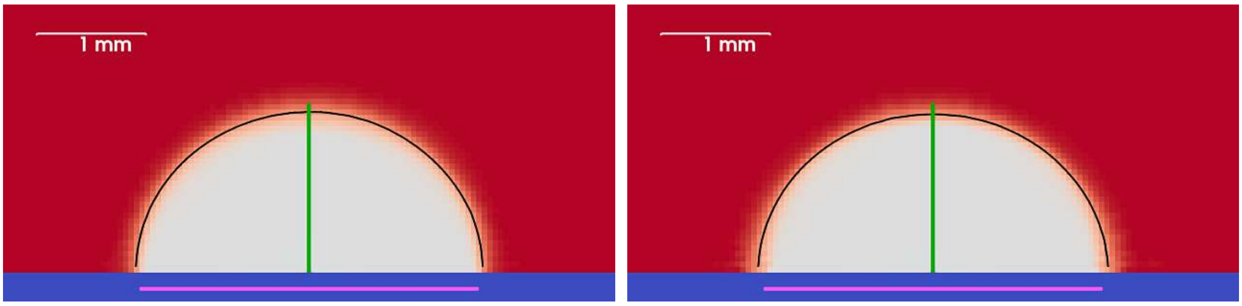

(c) $\theta = 90°$, tensor-based (T)

(d) $\theta = 90°$, decomposed tensor-based ($\mathrm{T_d}$)

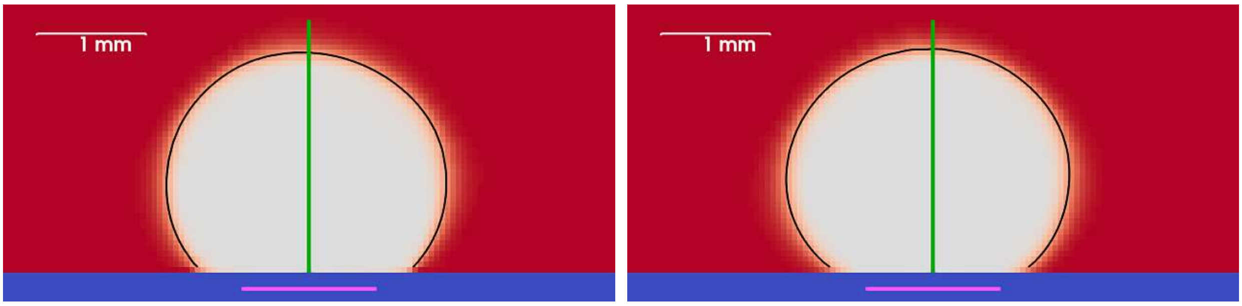

(e) $\theta = 150°$, tensor-based (T)

(f) $\theta = 150°$, decomposed tensor-based ($\mathrm{T_d}$)

Figure 6.10: Steady-state droplet shapes of the tensor-based models with the liquid boundary $\alpha_L = 0.5$ marked by the black contour. The magenta and green lines refer to the theoretical base diameter and droplet height, respectively.

The inaccuracy of the tensor-based model is immediately recognizable. For hydrophilic surfaces, the actual contact angle is larger, while for hydrophobic surfaces it is smaller than the theoretical contact angle. The model provides 45° instead of 30° (see Figure 6.10a) and 135° instead of 150° (see Figure 6.10e). The problem does not occur at 90° and the results match the theoretical solutions quite well. A detailed analysis of the problems with respect to curvature and triple line forces is provided in Appendix A, where the inaccuracies of the tensor-based model are explained using simple cases.

The inaccuracy of the tensor-based model can be corrected using the surface tension decomposition method ($\mathrm{T_d}$). It works for these cases, because there are only three phases. Unlike the shared phase gradient, the single phase gradients end at the domain boundary. These continuous functions without any jump ensure the correct handling of the triple line. The contact angle is generated due to the ratio between the phase specific surface tension coefficients. Table 6.5 contains these coefficients calculated from the values of Table 6.4. The value of σ_S is negative in all three cases. As the solid interface is straight, this value is insignificant. However, σ_L and σ_G show the wetting scenario. σ_G is dominant for hydrophilic wetting, while σ_L is larger for hydrophobic wetting, and the two are equal for a contact angle of 90°.

Table 6.5: Decomposed surface tension coefficients to achieve the given contact angles.

contact angle θ (°)	σ_S (N/m)	σ_L (N/m)	σ_G (N/m)
30	$-4.55 \cdot 10^{-3}$	$4.88 \cdot 10^{-3}$	$6.79 \cdot 10^{-2}$
90	$-1.82 \cdot 10^{-2}$	$3.64 \cdot 10^{-2}$	$3.64 \cdot 10^{-2}$
150	$-4.55 \cdot 10^{-3}$	$6.79 \cdot 10^{-2}$	$4.88 \cdot 10^{-3}$

Figures 6.10b, 6.10d and 6.10f (right column) show the results with surface tension decomposition. The steady-state droplet shape looks better and is more consistent with the theoretical one.

However, there is another problem that applies to both models and generally characterizes the tensor-based models. When averaging the maximum velocities of each time step over time, an interesting tendency can be observed. As Table 6.6 shows, the average velocity is unphysically high for small contact angles and decreases with larger contact angles. The high velocities typically occur in the gas phase and seem to be proportional to the surface tension coefficients acting on the gas phase. These coefficients are always larger for small contact angles.

Table 6.6: Averaged maximum velocities of the tensor-based models for the three contact angles.

	$\overline{u_{max}}$ (m/s)	
contact angle θ (°)	tensor-based (T)	decomp. tensor-based ($\mathrm{T_d}$)
30	11.30	9.16
90	3.97	3.94
150	0.93	0.94

6.4.5 Vector-Based Models

The three simulations were also run with the vector-based models. The results using the original vector-based model (V1) are shown in Figures 6.11a, 6.11c and 6.11e (left column). The result using the modified vector-based model (V2) can be seen in Figures 6.11b, 6.11d and 6.11f (right column). Both models are very accurate and are in good agreement with the theoretical base diameter and height of the droplet. They are very similar, however, the modified vector-based model provides smoother interfaces. Looking at the averaged maximum velocities (Table 6.7), it is clear that the high velocities of the tensor-based models do not occur using the vector-based models. Moreover, the modified vector-based model has even smaller velocities compared to the original vector-based model.

Table 6.7: Averaged maximum velocities of the vector-based models for the three contact angles.

	$\overline{u_{max}}$ (m/s)	
contact angle θ (°)	vector-based (V1)	modified vector-based (V2)
30	0.82	0.28
90	0.66	0.65
150	0.75	0.18

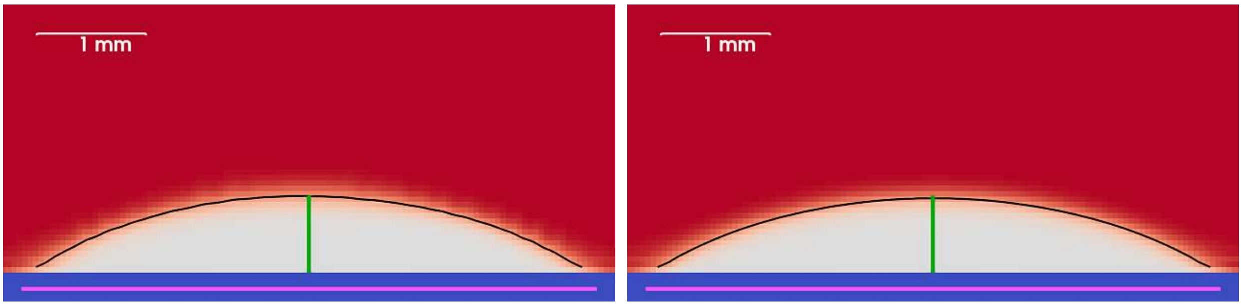

(a) $\theta = 30°$, vector-based (V1)   (b) $\theta = 30°$, modified vector-based (V2)

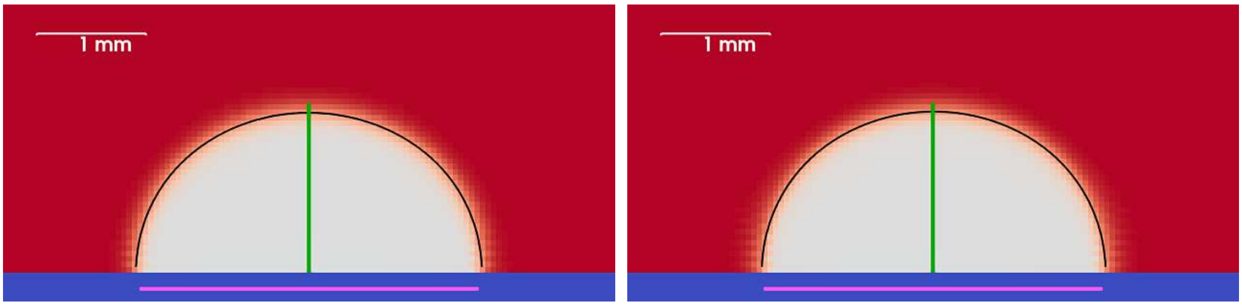

(c) $\theta = 90°$, vector-based (V1)   (d) $\theta = 90°$, modified vector-based (V2)

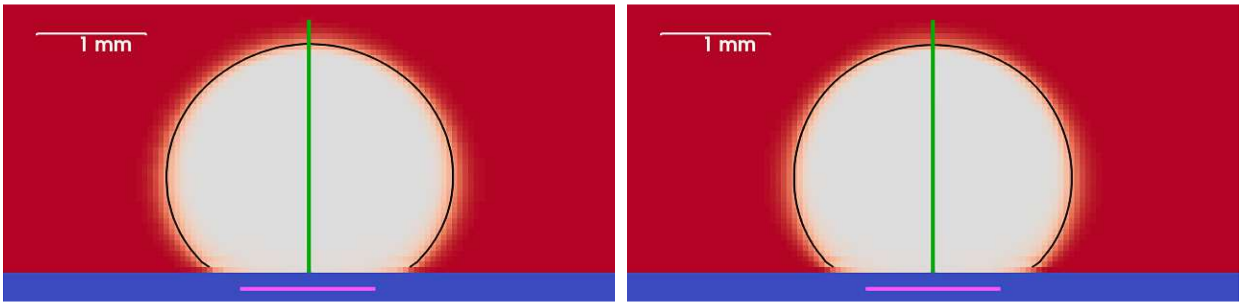

(e) $\theta = 150°$, vector-based (V1)   (f) $\theta = 150°$, modified vector-based (V2)

Figure 6.11: Steady-state droplet shapes of the vector-based models with $\alpha_L = 0.5$ marked by the black contour. The magenta and green lines refer to the theoretical base diameter and droplet height, respectively.

6.5 Droplet on Laser-Structured Surface

Skrna [2] performed experiments on laser-structured stainless steel surfaces. In the following simulations, surface number 3 from that work was used, which is shown in Figure 6.12. The surface was generated using a femtosecond laser system with a spot diameter of 50 µm. More details can be found in the work by Fürbacher et al. [28].

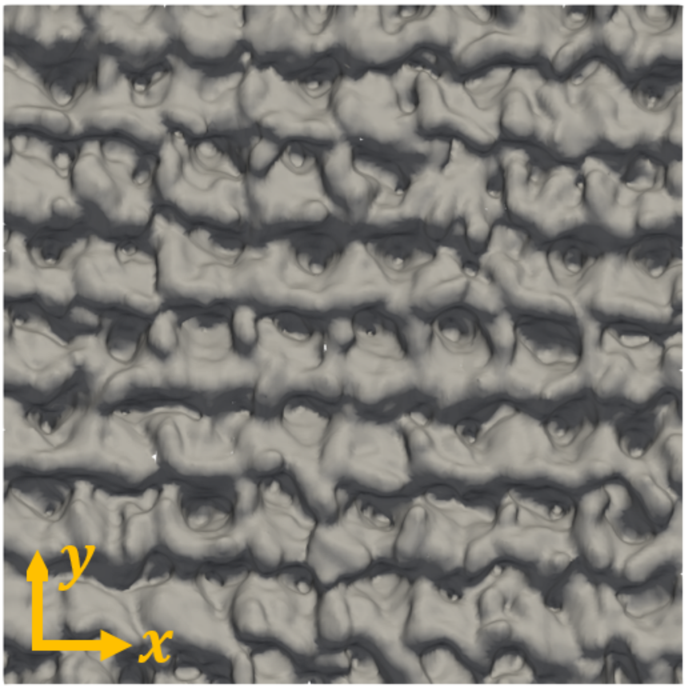

(a) Top view

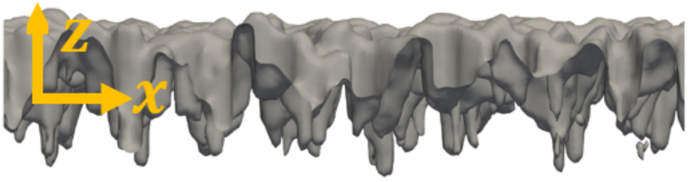

(b) Side view

Figure 6.12: The laser-structured surface used in the simulations.

6.5.1 Surface Tension Model

Because the modified vector-based model (V2) worked very well in the flat surface simulations, this model was chosen for the laser-structured surface simulations. However, the equation of the surface tension force was slightly modified. The reason for this was the curved solid surface, where the curvature forces were to be excluded. Since surface tension models calculate forces acting at the interface between two phases, both phases are accelerated and the velocities in the non-solid phase become high. Therefore, curvature forces were calculated only at the liquid-gas interface. The surface tension force used for the laser-structured surface reads

$$\boldsymbol{f}_{st} = \underbrace{-\sigma_{LG}\kappa_{LG}\nabla\alpha_{LG}}_{\text{Curvature force}} + \sum_{i=1}^{N}\sum_{j=i+1}^{N}\underbrace{2\sigma_{ij}(\nabla\alpha_i \times \nabla\alpha_j) \times \hat{\boldsymbol{n}}_{ij}}_{\text{Triple line force}} \tag{6.20}$$

with $N = 3$ in this case. Note that such a restriction is not possible with a surface tension model where the contribution of forces due to curvature to the overall surface tension forces is not separately recovered, e.g. with the tensor-based model.

6.5.2 Surface Tension Coefficients

In general, it is not obvious to find the surface tension coefficients for the laser-structured simulations. In case of flat surfaces, they are derived from the experimentally measured contact angle. Laser-structured surfaces, on the other hand, have a global and a local contact angle. The global contact angle depends on the geometry of the surface and can be obtained during an experiment, while the local contact angle is formed at the triple line and is not easy to determine. Simulations handle surface tension locally, thus it is necessary to find the local contact angle. A good procedure would be to determine the local contact angle from a flat surface experiment and set the corresponding surface tension coefficients in the laser-structured simulations.

Skrna observed that the contact angle also depends on when it was measured. It was found that the contact angle is different if the wetting is investigated directly after the production of the surface or after a certain period of time. The reason for that is that laser-structured surfaces absorb hydrocarbons from the surrounding air, which change hydrophilic surfaces to hydrophobic ones [28]. To avoid chemical effects, Skrna applied a 5 nm thin layer of platinum to both the flat and the laser-structured surfaces. Since the simulations were compared with experiments and water has a significant polar surface tension component, the OWRK method (Equation 3.6) was used to calculate the free surface energy between solid and liquid. The dispersion and polar surface tension components of water and the surface coated with platinum, and the free surface energy between them are listed in Table 6.8.

Table 6.8: Dispersion and polar components of water and the laser-structured surface, and the resulting free surface energy between them.

σ_{LG}^{D} (N/m)	σ_{LG}^{P} (N/m)	σ_{SG}^{D} (N/m)	σ_{SG}^{P} (N/m)	σ_{SL} (N/m)
$2.18 \cdot 10^{-2}$	$5.10 \cdot 10^{-2}$	$3.17 \cdot 10^{-2}$	$1.30 \cdot 10^{-3}$	$3.69 \cdot 10^{-2}$

6.5.3 Simulation

Simulations were performed with three different droplet diameters: 200 µm, 400 µm and 800 µm. Table 6.9 contains initial diameter, volume and Bond number of the three cases.

Table 6.9: Initial diameter, volume, and Bond number of the three simulations.

initial diameter D_0 (µm)	volume V_0 (µl)	Bond number
200	$4.19 \cdot 10^{-3}$	$5.39 \cdot 10^{-3}$
400	$3.35 \cdot 10^{-2}$	$2.16 \cdot 10^{-2}$
800	$2.68 \cdot 10^{-1}$	$8.62 \cdot 10^{-2}$

These droplet diameters were chosen for numerical reasons. Due to the difference in size between surface structure and droplet diameter, the simulation of the largest droplet consisted of cells with 5 different sizes (see Figure 6.13), resulting in a total cell number of around 10.7 million.

The experiments were performed with a droplet volume of 10 µl ($D_0 = 2.67$ mm). That means that the droplet diameter should have been increased by a factor of 3.34 in order to reproduce the experiments. Note that simulating a larger droplet needs a larger surface area and therefore more cells. Moreover, the time needed to perform simulations is further increased because the steady state is obtained later.

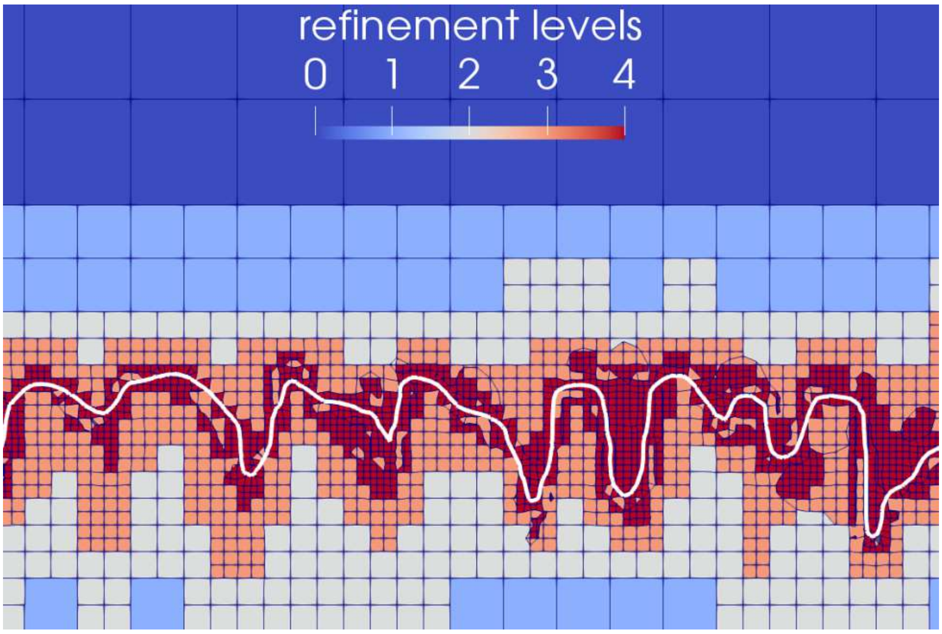

Figure 6.13: Refinement levels of the simulation with the largest droplet.

The Bond number was small in all three cases, so the droplet was expected to form a spherical cap (valid for $\mathrm{Bo} \ll 1$). However, the Bond number increases with the droplet diameter, which means that the droplets are not completely analogous. The steady-state solutions of the three simulations are shown in Figure 6.14.

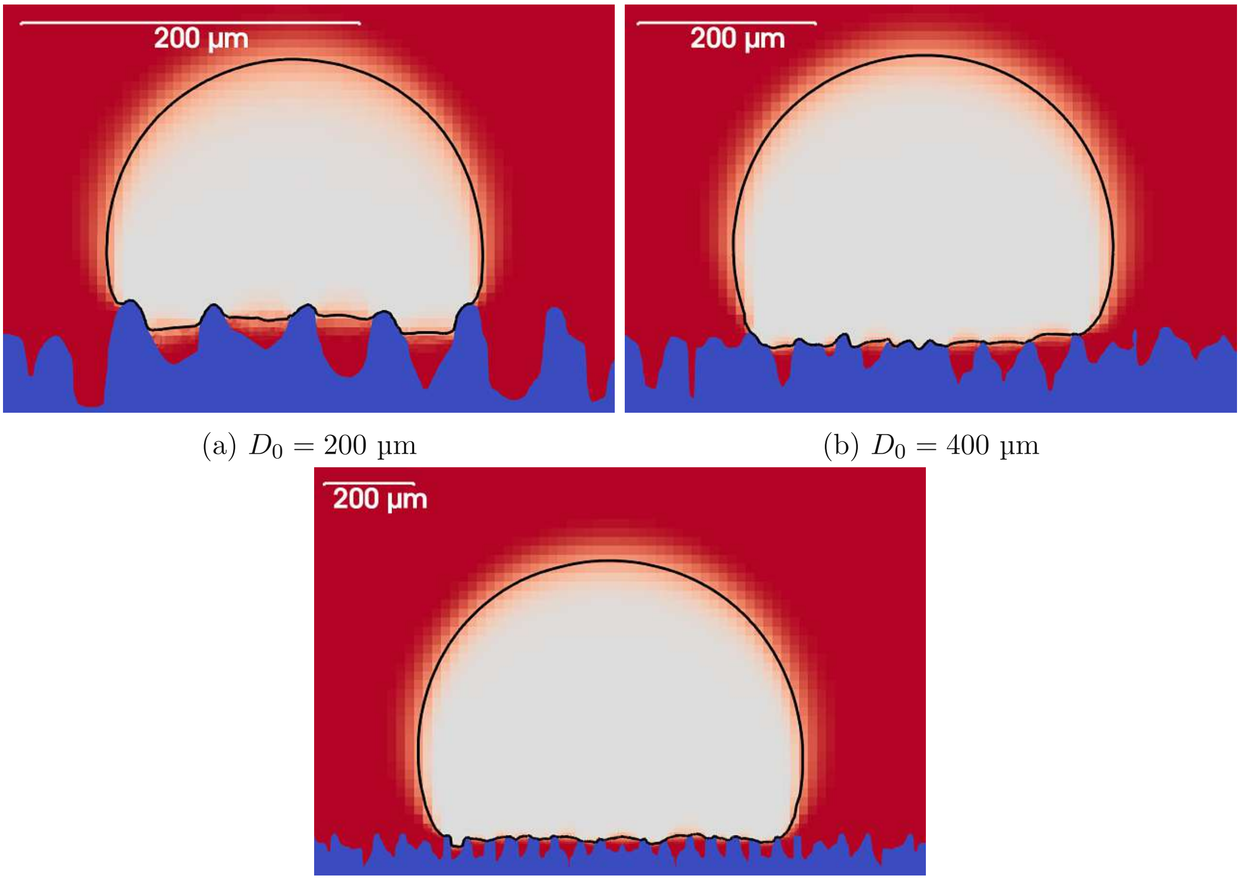

(a) $D_0 = 200$ µm (b) $D_0 = 400$ µm

(c) $D_0 = 800$ µm

Figure 6.14: Steady-state droplet shapes on the laser-structured surface of the three simulations with $\alpha_L = 0.5$ marked by the black contour.

The goal of the study was to observe the droplet size dependency of the resulting contact angle. Because the droplet was not absolutely symmetrical on the surface, the contact angle was measured in three different planes, which were rotated around the vertical axis. The contact angles were evaluated using the analytical solution for small Bond numbers. First, the height h, the width w and the base diameter d_b were measured in each plane, then the mean value was calculated. Table 6.10 contains the ratio height to base diameter h/d_b and the ratio width to base diameter w/d_b of each droplet. A contact angle was determined from each ratio. The two contact angles are given as a range in Table 6.11.

Table 6.10: Height to base diameter ratios and width to base diameter ratios of the three droplets.

initial diameter D_0 (µm)	height to base diam. h/d_b	width to base diam. w/d_b
200	0.75	1.04
400	0.88	1.15
800	0.83	1.14

Table 6.11: Comparison of contact angles resulting from experiments and simulations. The lower and upper bounds of the range in case of the simulations were determined from h/d_b and w/d_b, respectively.

	flat (experiment)	laser-str. (experiment)	$D_0 = 200$ µm (simulation)	$D_0 = 400$ µm (simulation)	$D_0 = 800$ µm (simulation)
θ (°)	93.2	155.2	[106,113]	[120,121]	[118,119]

The results show that the local contact angle of 93.2° leads to a larger global contact angle purely due to the surface geometry. However, the experimentally determined contact angle of the laser-structured surface is considerably larger than that found in the simulations.

The contact angles evaluated from h/d_b and w/d_b are significantly different for the smallest droplet. The reason for that is that the influence of the surface structure is larger in this case and the shape of the droplet is more dependent on the local structure of the surface. For the two larger droplet diameters, the two contact angles are similar, and increasing the droplet size affects the contact angle only slightly.

It should be mentioned that the Bond number increases with the droplet diameter. That means that gravity is more dominant for larger droplets, and the shape of the droplet is not exactly a spherical cap. Therefore, determining the contact angle from h/d_b and w/d_b for even larger droplets would lead to smaller contact angles, although the actual contact angle remains the same.

6.6 Icing on Laser-Structured Surface

If the temperature of the laser-structured surface is below melting temperature (0°), the water freezes to the plate. This phenomenon makes the simulations more complex, because equations of heat conduction, heat convection, and phase change also need to be solved. In the following, the simulation results of icing are presented on the same laser-structured surface as before.

The aim of the icing simulations was to investigate and understand the solidification process on laser-structured surfaces. Moreover, the focus was on the resulting steel-ice interface area, which is strongly related to the adhesive forces and therefore to the forces required to remove ice from the surface. This is important because if the force needed is low, the ice can fall off due to the forces occurring in the system, e.g. gravity, centrifugal force. Otherwise, the ice can become a larger block and damage its environment if it finally separates from the surface.

6.6.1 Material Properties

The material properties used in the simulations are listed in Table 6.12. It is important to emphasize the difference in density between ice and water, which leads to expansion during freezing.

Table 6.12: Material properties applied in the icing simulations.

Property	Value	Unit
Density (ice) ρ_I	916.2	kg m^{-3}
Density (water) ρ_W	1000	kg m^{-3}
Specific heat capacity (ice) $c_{p,I}$	2050	J kg^{-1} K^{-1}
Specific heat capacity (water) $c_{p,W}$	4220	J kg^{-1} K^{-1}
Thermal conductivity (ice) λ_I	2.22	W m^{-1} K^{-1}
Thermal conductivity (water) λ_W	0.56	W m^{-1} K^{-1}
Melting temperature T_M	0	°C
Latent heat of fusion L_{fusion}	$3.34 \cdot 10^5$	J kg^{-1}

Since the underlying numerical model is a mixture model, several phases share one cell. Therefore, the material properties of the phases present need to be averaged locally in each cell. The most important material property in this respect is thermal conductivity, as it has a significant influence on the results of icing simulations. The reason for this is the thermal conductivity of air (0.02 W/mK), which is considerably smaller than that of ice and water. In this work, two averaging methods are introduced and used.

In case of arithmetic averaging, thermal conductivity is averaged proportional to the phase volume fractions. This method is useful in the forming ice layer under the droplet. During freezing, small air particles remain in the cells filled mainly with ice, which reduce the thermal conductivity only slightly when arithmetic averaging is applied. In contrast, if the air phase volume fraction is larger, e.g. in cells filled with water and air around the droplet, arithmetic averaging is no longer valid. In these cells, harmonic averaging should be used, which shifts the averaged thermal conductivity towards that of air. For these reasons, a mixed averaging method depending on the phase volume fraction of air was used in the simulations:

$$\lambda_{arithmetic} = \sum_{i=1}^{N} \alpha_i \lambda_i \ , \qquad \text{if} \quad \alpha_{air} \leq 0.5 \ , \tag{6.21}$$

$$\lambda_{harmonic} = \left(\sum_{i=1}^{N} \frac{\alpha_i}{\lambda_i} \right)^{-1} \ , \qquad \text{if} \quad \alpha_{air} > 0.5 \ . \tag{6.22}$$

6.6.2 Surface Tension Model

The surface tension model was the modified vector-based model (V2) as in the simulations without freezing (Equation 6.20). The only difference was that having $N = 4$ phases (steel, ice, water, air) instead of 3 leads to a number of phase pairs of 6 instead of 3. Curvature forces were only included at the water-air interface. However, when calculating the triple line forces, some restrictions were necessary.

First, the triple line forces of all phase pairs with water (steel-water, ice-water, water-air) were considered completely, as water was the most important phase in terms of droplet shape and contact angle formation. Second, the triple line forces of the phase pair steel-ice were neglected. This was crucial, because during freezing, the steel-ice triple line forces would also act in cells shared by ice, water, and air. In these cells, the solid movement restriction term is weaker than in fully solid cells, which would lead to an unnecessary movement of the phases. Third, the triple line forces of the steel-air and ice-air phase pairs were only calculated in cells that contained at least some water. At an interface between two phases, $\nabla\alpha_1$ and $\nabla\alpha_2$ are parallel and the cross product results in a zero vector, therefore the triple line forces are zero. However, if three phases are present and none of them is water, e.g. at the steel surface after a layer of ice has formed, triple line forces occur. These forces accelerate both ice and air in already frozen regions. Note that the triple line forces of the steel-air and ice-air phase pairs are important in the formation of the water contact angle and cannot be neglected completely. The threshold value above which these forces were included in the calculation was $\alpha_W = 10^{-3}$.

6.6.3 Surface Tension Coefficients

The surface tension coefficients of water and the laser-structured surface were the same as in the previous simulations. The dispersion and polar components of free surface energy of ice were evaluated by Kloubek [7] by analyzing several different experiments. It was found that ice, unlike water, has a nonpolar character. The components of the three phases are summarized in Table 6.13. Based on the components, the local contact angle between steel and water was 93.2°, and 24.5° between ice and water.

Table 6.13: Dispersion and polar components of water, the laser-structured surface, and ice.

σ_W^D (N/m)	σ_W^P (N/m)	σ_S^D (N/m)	σ_S^P (N/m)	σ_I^D (N/m)	σ_I^P (N/m)
$2.18 \cdot 10^{-2}$	$5.10 \cdot 10^{-2}$	$3.17 \cdot 10^{-2}$	$1.30 \cdot 10^{-3}$	$9.46 \cdot 10^{-2}$	$1.14 \cdot 10^{-2}$

6.6.4 Interface Detection

The interfaces between two phases were identified from their volume fractions. Both phase volume fractions were linearly interpolated on the cell faces and multiplied with each other. Two phase pairs were of key importance when analyzing the freezing of the droplets, the steel-water (SW) and the steel-ice (SI) interfaces:

$$I_{SW} = \alpha_{S,f} \cdot \alpha_{W,f} \ , \qquad I_{SI} = \alpha_{S,f} \cdot \alpha_{I,f} \ . \tag{6.23}$$

The steel-water interface function was used to find the point when there is no more water in contact with the surface and thus a full ice layer has formed. The steel-ice interface function contributed to determining the steel-ice interface area. Figure 6.15 illustrates two examples on the steel surface. In multiphase simulations, the boundary of a phase is marked at $\alpha = 0.5$. This value corresponds to an interface function value of 0.125 (see Figure 6.15).

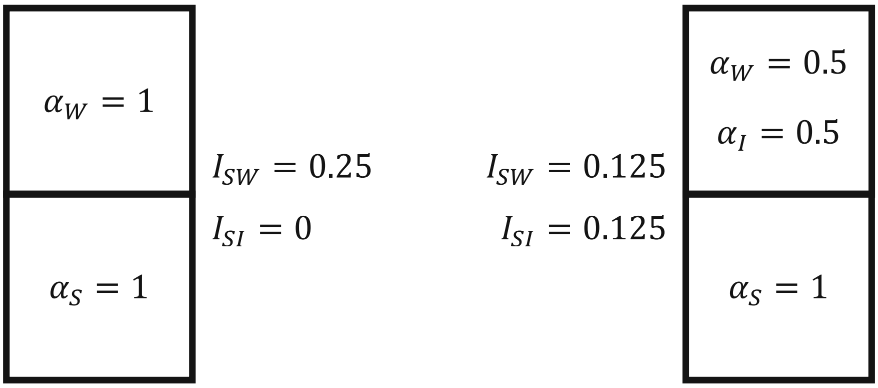

Figure 6.15: Example cases of calculating the steel-water interface function I_{SW} and the steel-ice interface functions I_{SI} as defined in Equation 6.23.

6.6.5 Effect of Solid Movement Restriction

As discussed in Section 4.2, the original equation of the solid movement restriction term has the form

$$\boldsymbol{S}_{D,1} = -\frac{\mu}{A_{perm}} \underbrace{\frac{\alpha_S^2}{(1-\alpha_S)^3+\delta}}_{k_1} \boldsymbol{u} \ . \tag{6.24}$$

Modeling the term in this way resulted in significant diffusion of ice at both the ice-water and ice-air interfaces (see Figure 6.17a). For that reason, the term was modified by applying the square root function instead of the square function in the numerator:

$$\boldsymbol{S}_{D,2} = -\frac{\mu}{A_{perm}} \underbrace{\frac{\sqrt{\alpha_S}}{(1-\alpha_S)^3+\delta}}_{k_2} \boldsymbol{u} \ . \tag{6.25}$$

Since the solid volume fraction is in the range $0-1$, this modification led to a larger value of $\boldsymbol{S}_D$, especially in cells with a small ice volume fraction. Figure 6.16 illustrates the functions k_1 and k_2, i.e. $\boldsymbol{S}_D$ without the contributions of μ, A_{perm}, and $\boldsymbol{u}$.

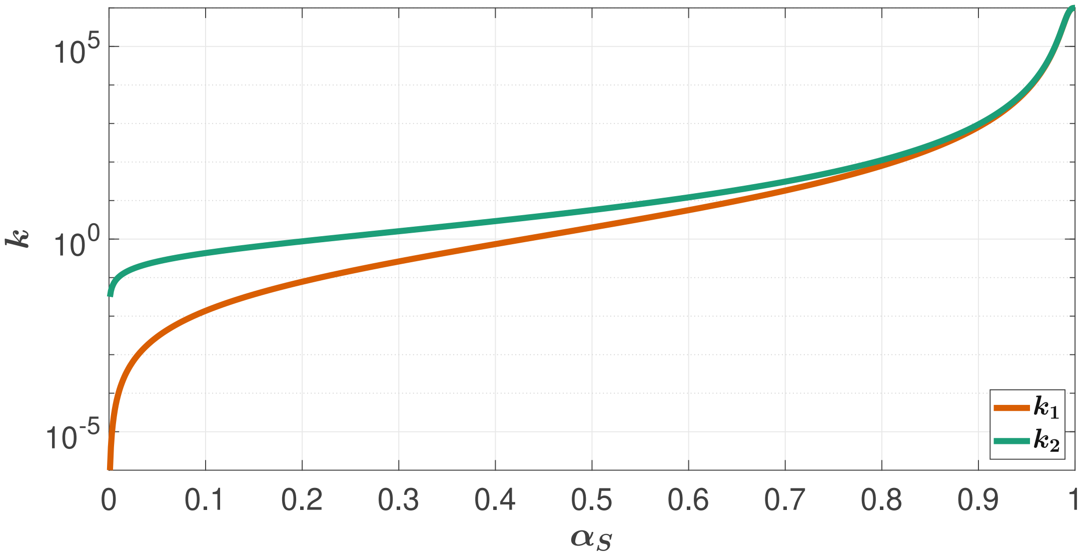

Figure 6.16: Original (k_1) and modified (k_2) solid movement restriction terms over the solid phase fraction.

Figure 6.17 compares the results with the two solid movement restriction terms. Indeed, $\boldsymbol{S}_{D,2}$ reduces the diffusion around ice, both towards water and air. As a consequence, less diffusion also means that the phase boundary $\alpha_I = 0.5$ is further up and therefore the steel-ice interface area is smaller.

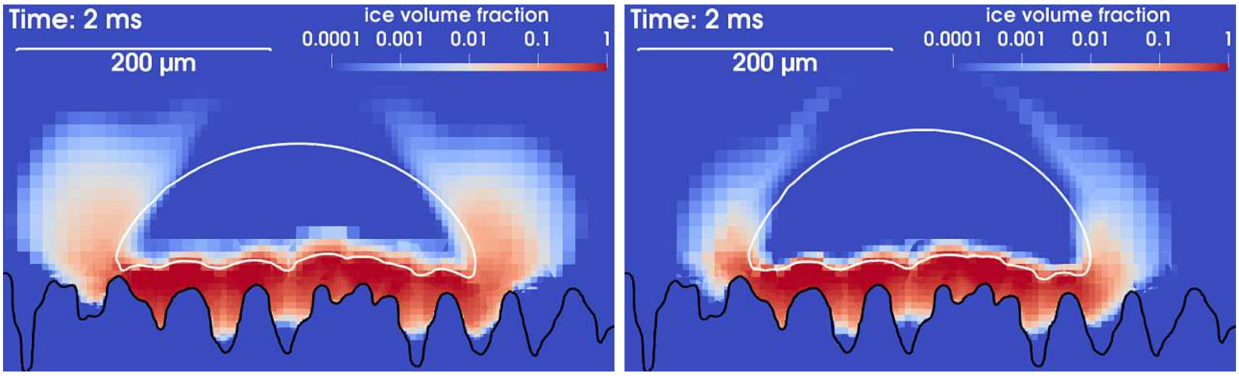

(a) $\boldsymbol{S}_{D,1}$ (b) $\boldsymbol{S}_{D,2}$

Figure 6.17: Dependence of the ice diffusion on the choice of the solid movement restriction term.

Figure 6.18 shows the resulting interface area in the x direction with $\boldsymbol{S}_{D,1}$ and $\boldsymbol{S}_{D,2}$. Note that when choosing a function for $\boldsymbol{S}_D$, a compromise must be made. On the one hand, if $\boldsymbol{S}_D$ is too large for small α_S values, the fluid flow is also affected by it. On the other hand, if $\boldsymbol{S}_D$ is too small, the solid phases diffuse strongly.

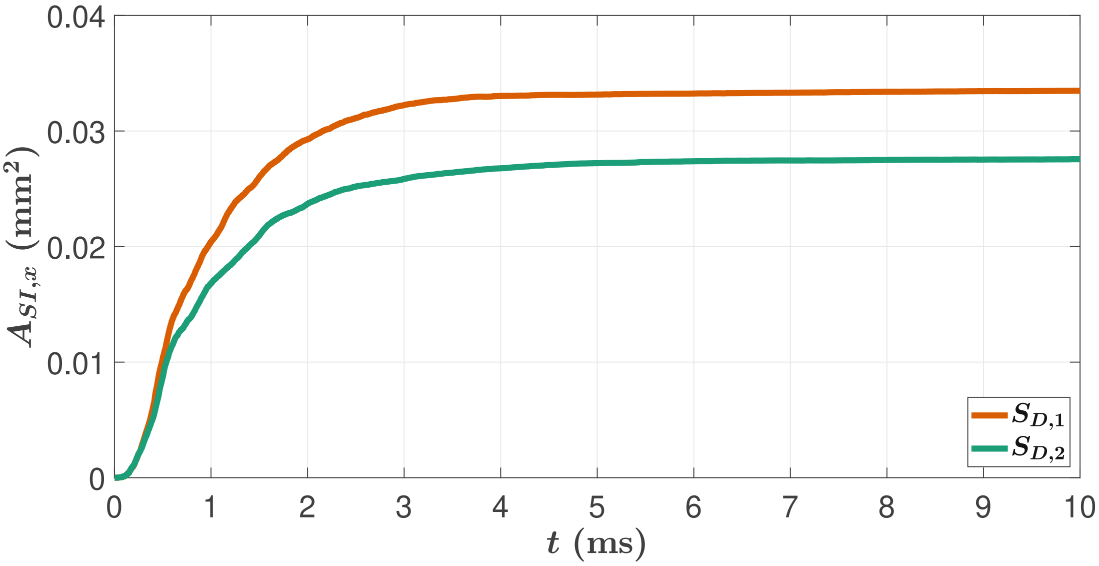

Figure 6.18: Steel-ice interface area in x direction $A_{SI,x}$ over time for the two solid movement restriction terms.

6.6.6 Simulation

As in the previous section, simulations were performed with three different initial droplet diameters: 200 µm, 400 µm and 800 µm. The initial temperature of the laser-structured surface was −30°C, while it was 1°C for both water and air to prevent applying melting temperature as an initial condition.

During the simulation, the maximum of the steel-water interface function was measured. When this function drops to zero, there are no cells adjacent to the steel cells consisting of any water. That means that a full ice layer has formed at this point. The analysis of the simulation results is demonstrated on the example of the smallest droplet with $D_0 = 200$ µm. Figure 6.19 shows the maximum of the steel-water interface function in the domain and the steel-ice interface area in the x and y directions. The maximum of the steel-water interface function drops to zero at 5 ms. It can be seen that the steel-ice interface areas are constant after this point. The projection of the area in the x direction is smaller than in the y direction, which is due to the difference in the surface structure in the two directions resulting from the laser manufacturing process (see Figure 6.12a). The directional dependence of the steel-ice surface area is an interesting observation from the simulations and an important aspect to consider when applying the laser-structured surface to a component.

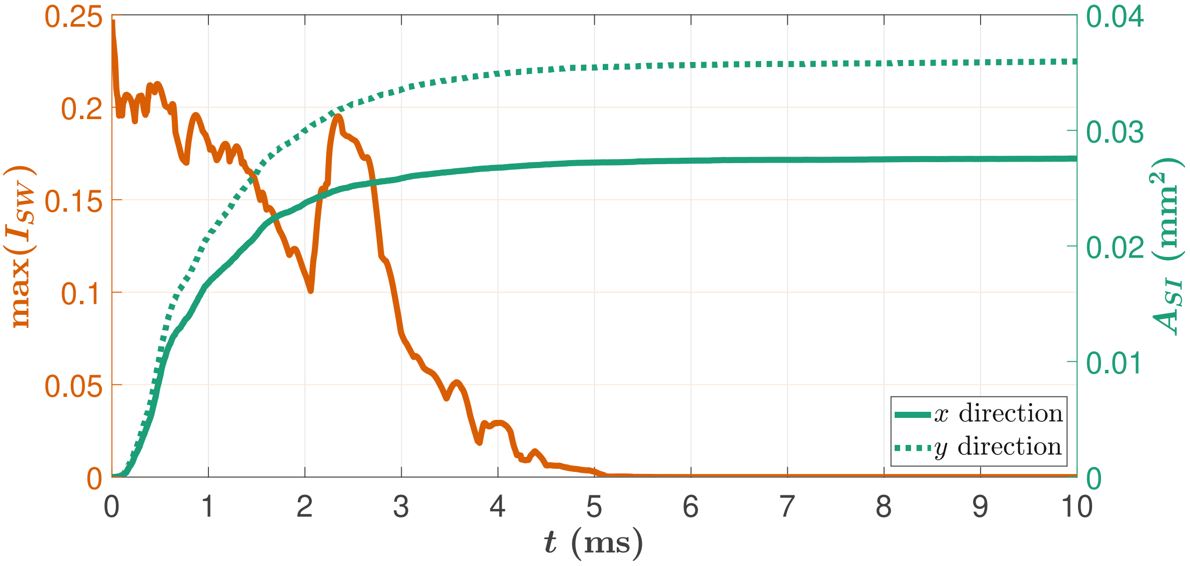

Figure 6.19: Maximum of the steel-water interface function I_{SW} and steel-ice interface area A_{SI} in x and y directions of the smallest droplet over time.

Table 6.14 contains the simulation results, while Figure 6.20 illustrates the phase distributions for all three droplet diameters. The time for the formation of a full ice layer increases with the diameter, following an approximately linear correlation. The reason for this is that the energy of the droplet scales with D_0^3, while the contact area where it is conducted into the solid scales with D_0^2.

The steel-ice interface area also grows linearly with the diameter in both directions. That means that the interface area decreases in relation to the droplet size (see Table 6.15), i.e. there is relatively less ice in the dimples, as shown in Figure 6.20. This tendency was also observed in the simulations without freezing. Less contact area also means less heat transfer between steel and water, and later between steel and ice. Moreover, the temperature of the laser-structured surface is less affected by the higher droplet temperature.

Table 6.14: Time for formation of a full ice layer, and steel-ice interface areas in x and y directions of the three simulations.

initial diameter D_0 (µm)	time for formation of a full ice layer τ (ms)	steel-ice interface area in x direction $A_{SI,x}$ (mm^2)	steel-ice interface area in y direction $A_{SI,y}$ (mm^2)
200	5	0.028	0.036
400	10	0.076	0.093
800	15	0.183	0.219

Table 6.15: Steel-ice interface areas in x and y directions of the three simulations in relation to the initial droplet surface area A_0.

initial diameter D_0 (µm)	$A_{SI,x}/A_0$	$A_{SI,y}/A_0$
200	0.219	0.286
400	0.151	0.184
800	0.091	0.109

The ice layer that has formed at time τ has a thickness of around 50 µm in all cases (see Figure 6.20). This thickness corresponds to a larger ice to water volume ratio for the smallest droplet than for the larger droplets. Figure 6.20 also shows the phenomenon observed in the simulations without freezing: The smallest droplet is more affected by the local surface structure, which can be recognized by the uneven freezing phase front. In case of the larger droplets, the local surface irregularities can be neglected with regard to the droplet size which results in a symmetrical freezing process.

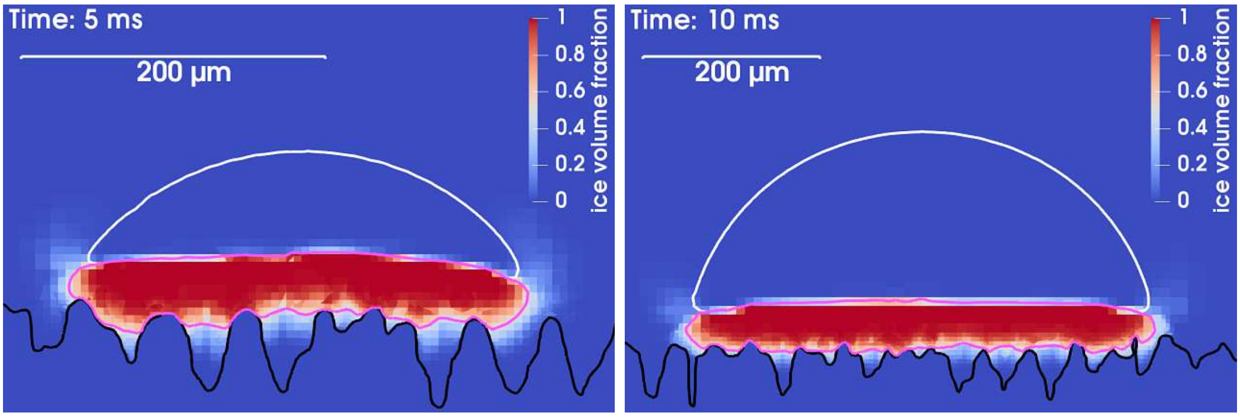

(a) $D_0 = 200$ µm (b) $D_0 = 400$ µm

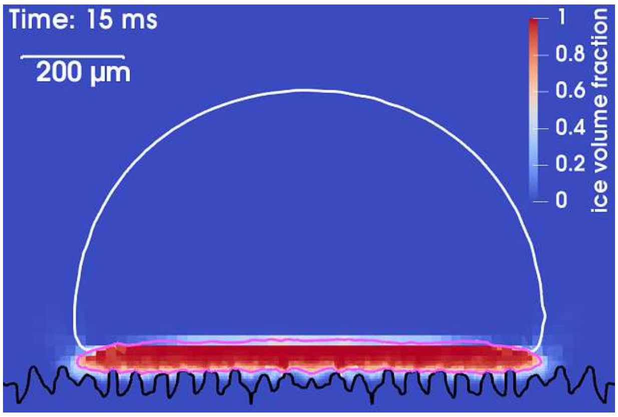

(c) $D_0 = 800$ µm

Figure 6.20: Ice volume fraction after the formation of a full ice layer on the laser-structured surface of the three simulations with $\alpha_W = 0.5$ marked by the white contour, $\alpha_S = 0.5$ marked by the black contour, and $\alpha_I = 0.5$ marked by the magenta contour.

7 Conclusion and Outlook

The goal of this study was to investigate different surface tension models and their numerical implementations in a multiphase solver. Two models, the tensor-based and the vector-based models were analyzed in detail. However, it was shown that their modifications and the numerical way of adding the surface tension force to the governing equations affect the results. One of these surface tension force models was found to be very accurate and applicable for simulating wetting and freezing of water droplets on laser-structured surfaces.

During the analysis, important characteristics of the surface tension force models were observed. The tensor-based model can be used if the solid surface is not extremely hydrophilic or hydrophobic. This inaccuracy is not dominant and can be neglected if other physical phenomena are more significant, e.g. in more dynamic processes. The vector-based model performed better when simulating extreme wetting conditions. Another advantage of the vector-based model was that the surface tension force consists of three terms with actual physical meaning. That means that surface tension forces on curved solid interfaces and undesired phase pairs could be excluded from the calculations.

The simulations of wetting on laser-structured surfaces were compared to experiments. It was an interesting observation that the geometry of the surface affects the resulting wetting condition. As a consequence, different local and global contact angles were observed. The local contact angle was that according to Young's equation (Equation 3.1), while the global contact angle was measured from a distance, without looking at the surface geometry. Although the local contact angle predicted neutral wetting, the global contact angle corresponded to a hydrophobic condition. However, the simulations underestimated the contact angles measured in the experiments. The reason for this may be that the droplet size was smaller in the simulations than in the experiments. The simulation of a larger droplet could be possible, but it would require a lot of computational capacity and time. Moreover, the test cases showed that the contact angle no longer increases above a certain droplet size. Thus, simulating even larger droplets will probably not solve the problem. An other possible reason may be the influence of the laser production process on the free surface energy of steel. To avoid this effect, a platinum coating was applied to the surfaces. The thickness of the coating could influence the results. It should be evenly distributed to exclude any chemical effects caused by the laser production, which is a challenging task for complex surface structures. In the future, these effects should be analyzed in order to gain a clearer understanding of the mechanism. Lastly, the resolution of the surface structure should be mentioned. For numerical reasons, the surface was simplified and smoothed after scanning. During this process, the surface roughness and small features were eliminated, resulting in a more regular surface than in reality. In future simulations, the influence of a more detailed surface structure should be analyzed in detail.

As a next step, the robustness of the simulation should be investigated systematically. Changing the initial position of the droplet in both the horizontal and vertical directions would serve as a good test to check if there are any inconsistencies in the modeling. Furthermore, the wetting and icing simulations should be run with the real droplet dimensions. The mesh of such a simulation would consist of around 100 million cells and would take several weeks to complete on the computer architecture used in the present work. For this purpose, the use of a scientific cluster with several hundred processors could be a suitable solution. However, once the contact angle was determined with a high-resolution simulation, and the actual laser-structured surface geometry is not important, it can be excluded from the simulation domain and replaced by a contact angle boundary condition. Therefore, the number of phases would be one less, and the number of cells would also decrease enormously.

There are many interesting tests regarding the wetting of water droplets, which could be performed using the developed models. First, the dynamic process of the droplet movement should be examined. Comparing the simulations with high speed recordings from experiments would help to better understand and validate the simulations. Second, wetting on an inclined solid surface is of key importance [28]. In reality, most cases occur on inclined surfaces, where gravity plays a different role and strongly influences the wetting and icing of the surface. Third, droplet impact with an initial velocity leads to more complex physical phenomena. At a certain velocity, the droplet may even disintegrate.

Similar to wetting, the icing of laser-structured surfaces also has a great potential. All of the tests mentioned above could be performed at a surface temperature below zero to induce freezing of the droplet. In addition, it would be interesting to see whether the surface area between steel and ice decreases further for larger droplets. As for wetting, a comparison with experiments would be beneficial. These investigations would contribute to the further development of the models and provide a more detailed insight into the physical processes.

A Appendix: Analysis of the Tensor-Based Model

Starting from the surface tension tensor, surface tension force can be calculated as (Section 4.3)

$$\boldsymbol{f}_{st}^{T} = \nabla \cdot \left[\sum_{i=1}^{N} \sum_{j=i+1}^{N} \sigma_{ij} (\mathbf{I} - \hat{\boldsymbol{n}}_{ij} \otimes \hat{\boldsymbol{n}}_{ij}) |\nabla \alpha_{ij}| \right] . \tag{A.1}$$

This formulation has some disadvantages that will be intuitively shown in this section. In the following examples, the focus is on the liquid-gas interface, where the surface tension forces can be evaluated as

$$\boldsymbol{f}_{st,LG}^{T} = \nabla \cdot \left[\sigma_{LG} (\mathbf{I} - \hat{\boldsymbol{n}}_{LG} \otimes \hat{\boldsymbol{n}}_{LG}) |\nabla \alpha_{LG}| \right] . \tag{A.2}$$

A.1 Curvature Forces

This problem is demonstrated using a two-dimensional sharp 90 degree corner between two phases (liquid and gas) shown in Figure A.1. This example corresponds to an extreme case of a water droplet surrounded by air. The small rectangle represents the area of interest where the detailed numerical analysis is performed in the following.

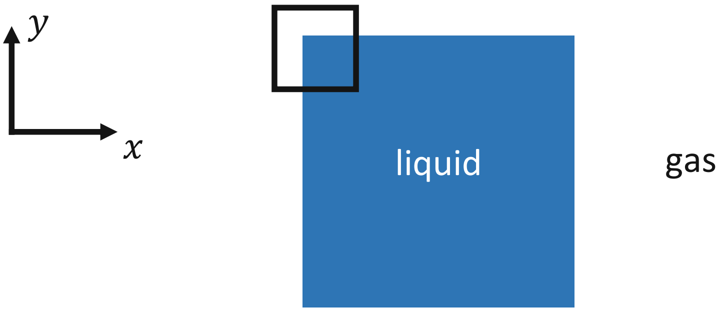

Figure A.1: Example case for the demonstration of curvature forces.

The rectangle consists of 3 cells both in x and y directions. Figure A.2a shows the volume fractions of liquid and gas. The phase gradients $\nabla \alpha_L$ and $\nabla \alpha_G$ can be calculated from the phase fractions. In numerical analysis, the method of central differences is suitable for the approximation of discrete derivatives. In this two-dimensional case for the scalar field α it reads

$$\nabla \alpha = \begin{bmatrix} \frac{\partial \alpha}{\partial x} \\ \frac{\partial \alpha}{\partial y} \end{bmatrix} \approx \begin{bmatrix} \frac{\alpha_{i+1} - \alpha_{i-1}}{2\Delta x} \\ \frac{\alpha_{j+1} - \alpha_{j-1}}{2\Delta y} \end{bmatrix} \tag{A.3}$$

with the cell indices i and j in x and y directions, respectively. In case of square cells $\Delta x = \Delta y$.

From $\nabla\alpha_L$ and $\nabla\alpha_G$ the shared phase gradient $\nabla\alpha_{LG}$ can be calculated using Equation 4.17:

$$\nabla\alpha_{LG} = \alpha_G\nabla\alpha_L - \alpha_L\nabla\alpha_G \, . \tag{A.4}$$

Figure A.2b illustrates the shared phase gradient, that represents the surface density function and thus also the liquid-gas interface. Therefore, surface tension forces should act only in these cells.

Using the previously obtained fields, the surface tension tensor on the liquid-gas interface $\mathbf{T}_{LG} = \sigma_{LG}(\mathbf{I} - \hat{\boldsymbol{n}}_{LG} \otimes \hat{\boldsymbol{n}}_{LG})|\nabla\alpha_{LG}|$ can be evaluated. The unitary normal vector $\hat{\boldsymbol{n}}_{LG}$ of the interface is calculated as the normalized shared phase gradient according to Equation 4.18. Figure A.2c shows the resulting surface tension tensor field.

Finally, the surface tension force is the divergence of the surface tension tensor:

$$\boldsymbol{f}^{T}_{st,LG} = \nabla \cdot \mathbf{T}_{LG} \, . \tag{A.5}$$

In the same way as the gradient, the divergence operator is also approximated by the method of central differences:

$$\nabla \cdot \mathbf{T}_{LG} = \begin{bmatrix} \frac{\partial T_{xx}}{\partial x} + \frac{\partial T_{xy}}{\partial y} \\ \frac{\partial T_{yx}}{\partial x} + \frac{\partial T_{yy}}{\partial y} \end{bmatrix} \approx \begin{bmatrix} \frac{T_{xx,i+1} - T_{xx,i-1}}{2\Delta x} + \frac{T_{xy,j+1} - T_{xy,j-1}}{2\Delta y} \\ \frac{T_{yx,i+1} - T_{yx,i-1}}{2\Delta x} + \frac{T_{yy,j+1} - T_{yy,j-1}}{2\Delta y} \end{bmatrix} \, . \tag{A.6}$$

Figure A.2d shows the resulting surface tension force. Because of the numerical approximation of the divergence operator, an undesirable spurious force occurs in the top left cell acting on the gas phase. The magnitude of the force is the same as the one acting on the interface.

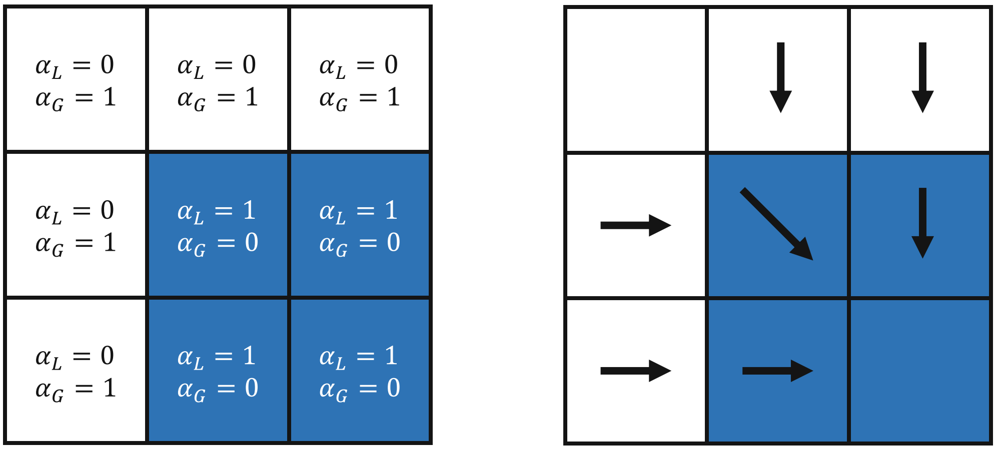

(a) Phase fractions α_L, α_G

(b) Shared phase gradient $\nabla\alpha_{LG}$

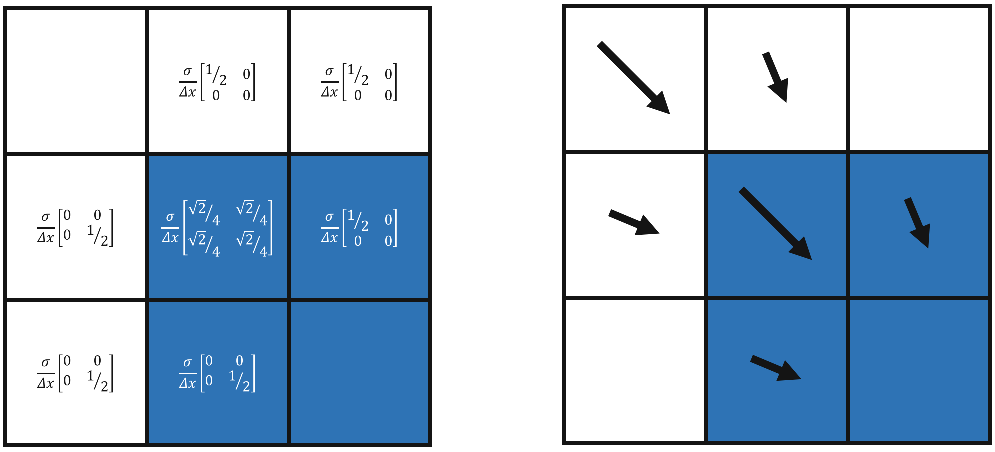

(c) Surface tension tensor $\mathbf{T}_{LG}$

(d) Surface tension force $\boldsymbol{f}^T_{st,LG}$

Figure A.2: Steps of the numerical analysis of the droplet case with the tensor-based model. Vectors are scaled by their magnitude. In (d), the spurious force occurs in the top left cell acting on the gas phase. For a more diffuse interface, the magnitude of the spurious forces is smaller.

Swapping the two phases results in a slightly different physical phenomenon. The case shown in Figure A.3a corresponds to e.g. a gas bubble in liquid. Because of the definition of the shared phase gradient, its vectors are opposite to the previous case. Since the operation $\hat{\boldsymbol{n}}_{LG} \otimes \hat{\boldsymbol{n}}_{LG}$ remains the same when $\hat{\boldsymbol{n}}_{LG}$ is rotated by 180° and the magnitude of the shared phase gradient $|\nabla\alpha_{LG}|$ is also unchanged, the surface tension tensor $\mathbf{T}_{LG} = \sigma_{LG}(\mathbf{I} - \hat{\boldsymbol{n}}_{LG} \otimes \hat{\boldsymbol{n}}_{LG})|\nabla\alpha_{LG}|$ and therefore the surface tension force $\boldsymbol{f}^T_{st,LG}$ are the same for the two cases (see Figure A.2d and Figure A.3d). However, the spurious force in the top left cell acts on the liquid phase.

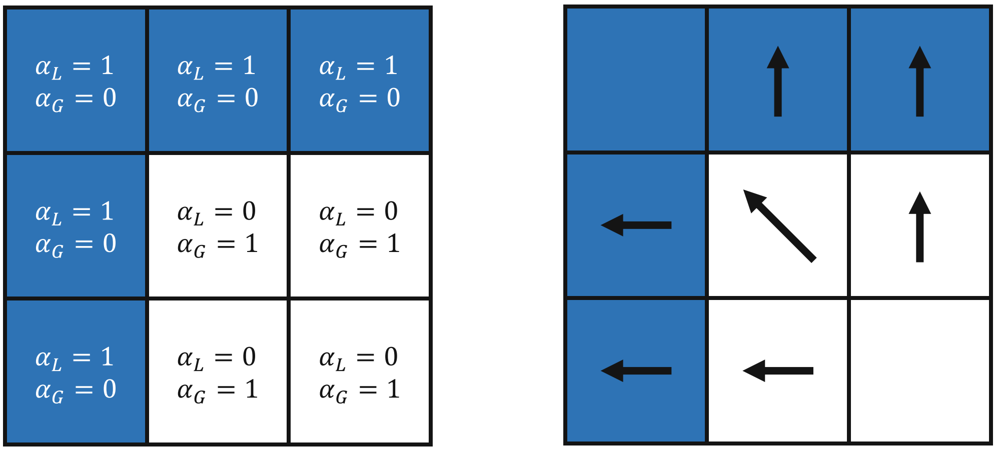

(a) Phase fractions α_L, α_G (b) Shared phase gradient $\nabla\alpha_{LG}$

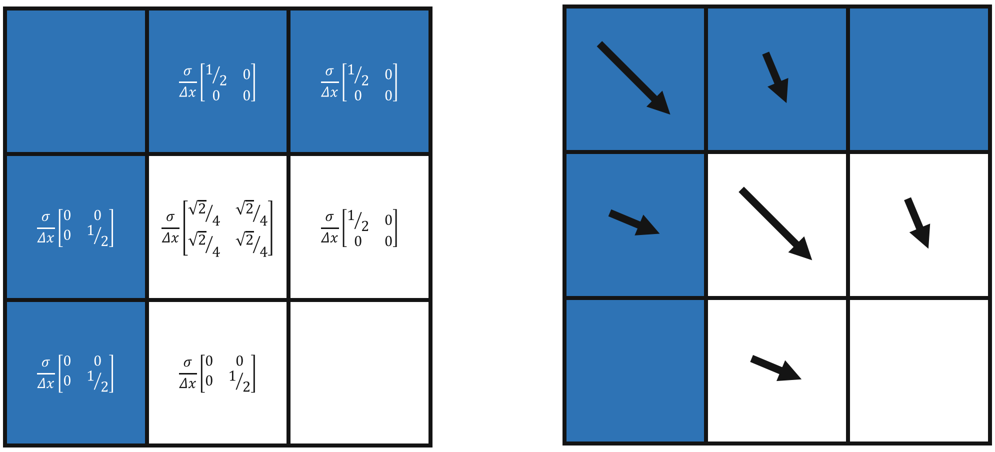

(c) Surface tension tensor $\mathbf{T}_{LG}$ (d) Surface tension force $\boldsymbol{f}^{T}_{st,LG}$

Figure A.3: Steps of the numerical analysis of the bubble case with the tensor-based model. Vectors are scaled by their magnitude. In (d), the spurious force occurs in the top left cell acting on the liquid phase. For a more diffuse interface, the magnitude of the spurious forces is smaller.

In general, when analyzing the treatment of curvature forces, following main features of the tensor-based model can be identified. The spurious forces act on the convex side of the curved interface. Besides, they occur in each cell adjacent to a curved interface. This is a problem because curvature in real simulations is represented by several cells (unlike in the previous simple examples), causing spurious forces in each of them. Additionally, as the magnitude of the spurious forces depends on the jump in the shared phase gradient, sharper interfaces cause larger spurious forces.

A.2 Triple Line Forces

An effect similar to the curvature problem arises at the triple line. The inaccuracy of the model regarding the triple line forces is demonstrated by the example of the liquid-gas interface, since surface tension forces on this interface are essential for the correct calculation of the contact angle.

In the example, a two-dimensional flat hydrophilic surface is considered where the contact angle is 45°. The liquid-gas interface is not curved, therefore there are no surface tension forces due to curvature. Figure A.4 illustrates the distribution of the phases and a small rectangle around the triple point for the numerical analysis.

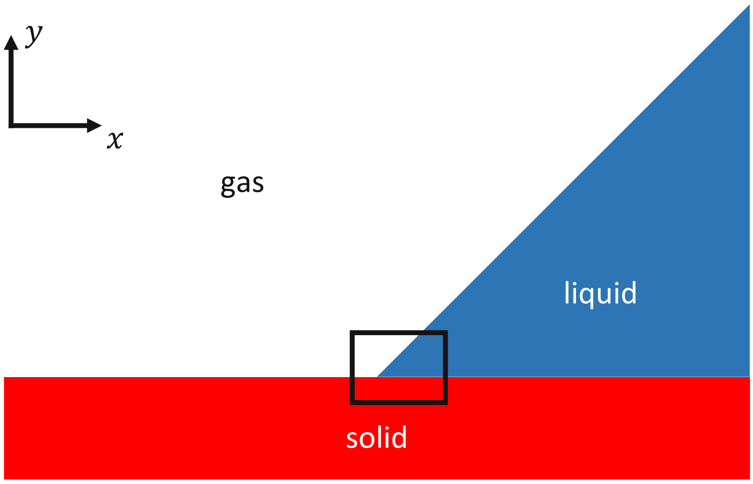

Figure A.4: Example case for the demonstration of triple line forces.

The rectangle consist of 4 cells horizontally and 3 cells vertically. Figure A.5a shows the volume fractions of solid, liquid, and gas. Cells with $\alpha_L = 0.5$ and $\alpha_G = 0.5$ are introduced on the liquid-gas interface to better represent the 45° contact angle.

As shown in Figure A.5b, the shared phase gradient points towards the liquid phase. Its magnitude is larger in the mixed cells, while smaller in the surrounding cells, corresponding to the surface density function described in Section 4.4. Note that the discrete approach extends the gradients also for cells beside the interface, i.e. for cells with only one phase. The first cell row in Figure A.5b shows what the liquid-gas gradient looks like away from the solid. However, near the solid, the gradient is affected by the solid cells and no longer follows the desired 45° angle.

Figure A.5c shows the surface tension tensor in each cell. Because of the multiplication by $|\nabla \alpha_{LG}|$, the tensor only takes values where the magnitude of the shared phase gradient is non-zero.

Figure A.5d shows the surface tension force on the liquid-gas interface. As a result of the shared phase gradient distorted by the solid phase, surface tension force in the middle cell row is not perfectly directed into the liquid-gas interface. In addition, the discrete approximation of the divergence operator causes spurious forces in the first cell row. Note that surface tension force vanishes in all cells apart from those shown in the figure, because the surface tension tensor components are either zero or are the same at least in two neighboring cells.

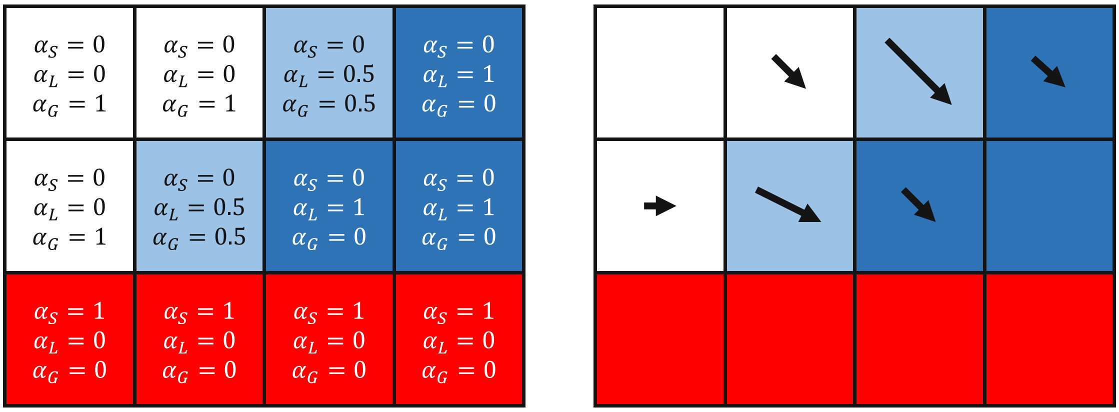

$\alpha_S = 0$ $\alpha_L = 0$ $\alpha_G = 1$	$\alpha_S = 0$ $\alpha_L = 0$ $\alpha_G = 1$	$\alpha_S = 0$ $\alpha_L = 0.5$ $\alpha_G = 0.5$	$\alpha_S = 0$ $\alpha_L = 1$ $\alpha_G = 0$
$\alpha_S = 0$ $\alpha_L = 0$ $\alpha_G = 1$	$\alpha_S = 0$ $\alpha_L = 0.5$ $\alpha_G = 0.5$	$\alpha_S = 0$ $\alpha_L = 1$ $\alpha_G = 0$	$\alpha_S = 0$ $\alpha_L = 1$ $\alpha_G = 0$
$\alpha_S = 1$ $\alpha_L = 0$ $\alpha_G = 0$	$\alpha_S = 1$ $\alpha_L = 0$ $\alpha_G = 0$	$\alpha_S = 1$ $\alpha_L = 0$ $\alpha_G = 0$	$\alpha_S = 1$ $\alpha_L = 0$ $\alpha_G = 0$

(a) Phase fractions α_S, α_L, α_G

(b) Shared phase gradient $\nabla\alpha_{LG}$

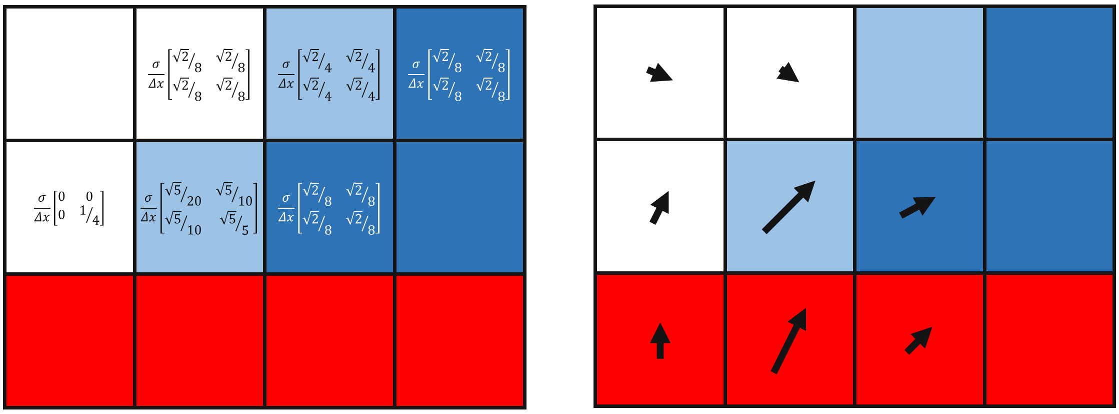

	$\frac{\sigma}{\Delta x}\begin{bmatrix}\sqrt{2}/8 & \sqrt{2}/8 \\ \sqrt{2}/8 & \sqrt{2}/8\end{bmatrix}$	$\frac{\sigma}{\Delta x}\begin{bmatrix}\sqrt{2}/4 & \sqrt{2}/4 \\ \sqrt{2}/4 & \sqrt{2}/4\end{bmatrix}$	$\frac{\sigma}{\Delta x}\begin{bmatrix}\sqrt{2}/8 & \sqrt{2}/8 \\ \sqrt{2}/8 & \sqrt{2}/8\end{bmatrix}$
$\frac{\sigma}{\Delta x}\begin{bmatrix}0 & 0 \\ 0 & 1/4\end{bmatrix}$	$\frac{\sigma}{\Delta x}\begin{bmatrix}\sqrt{5}/20 & \sqrt{5}/10 \\ \sqrt{5}/10 & \sqrt{5}/5\end{bmatrix}$	$\frac{\sigma}{\Delta x}\begin{bmatrix}\sqrt{2}/8 & \sqrt{2}/8 \\ \sqrt{2}/8 & \sqrt{2}/8\end{bmatrix}$	

(c) Surface tension tensor $\mathbf{T}_{LG}$

(d) Surface tension force $\boldsymbol{f}^{T}_{st,LG}$

Figure A.5: Steps of the numerical analysis of hydrophilic wetting with the tensor-based model. Vectors are scaled by their magnitude.

Steps of the numerical analysis of the bubble case with the tensor-based model. Vectors are scaled by their magnitude. In (d), the spurious force occurs in the top left cell acting on the liquid phase. For a more diffuse interface, the magnitude of the spurious forces is smaller.

Because of the definition of the contact angle, swapping the liquid and the gas phases corresponds to $\theta = 135°$ (see Figure A.6a). Figure A.6b shows the shared phase gradient, which consists of vectors opposite to the 45° case. For the reasons explained in the previous section, the surface tension tensor and the surface tension force are the same as for $\theta = 45°$. This behavior of the triple line forces generally applies to the contact angles θ_1 and $\theta_2 = 180° - \theta_1$.

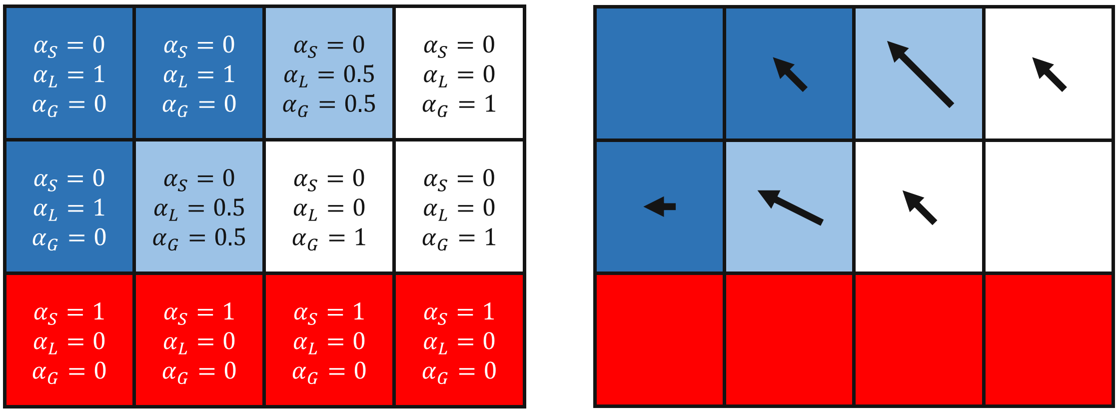

$\alpha_S = 0$ $\alpha_L = 1$ $\alpha_G = 0$	$\alpha_S = 0$ $\alpha_L = 1$ $\alpha_G = 0$	$\alpha_S = 0$ $\alpha_L = 0.5$ $\alpha_G = 0.5$	$\alpha_S = 0$ $\alpha_L = 0$ $\alpha_G = 1$
$\alpha_S = 0$ $\alpha_L = 1$ $\alpha_G = 0$	$\alpha_S = 0$ $\alpha_L = 0.5$ $\alpha_G = 0.5$	$\alpha_S = 0$ $\alpha_L = 0$ $\alpha_G = 1$	$\alpha_S = 0$ $\alpha_L = 0$ $\alpha_G = 1$
$\alpha_S = 1$ $\alpha_L = 0$ $\alpha_G = 0$	$\alpha_S = 1$ $\alpha_L = 0$ $\alpha_G = 0$	$\alpha_S = 1$ $\alpha_L = 0$ $\alpha_G = 0$	$\alpha_S = 1$ $\alpha_L = 0$ $\alpha_G = 0$

(a) Phase fractions α_S, α_L, α_G

(b) Shared phase gradient $\nabla \alpha_{LG}$

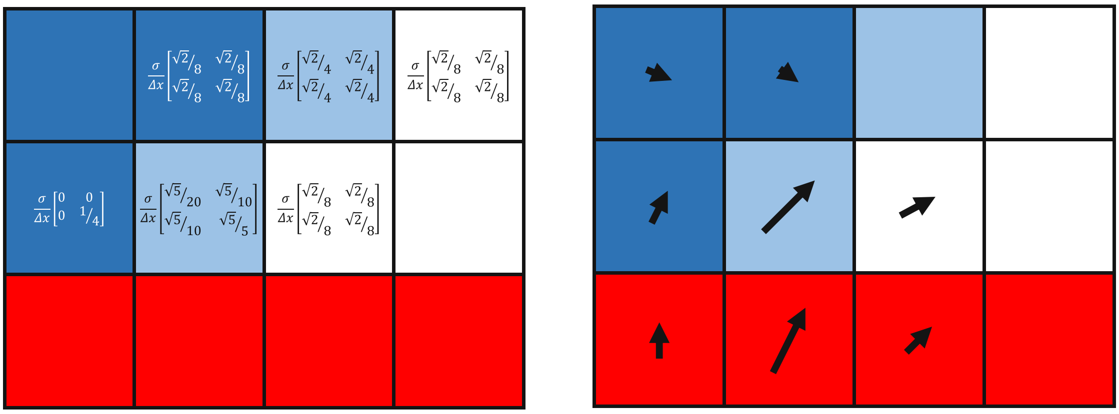

	$\frac{\sigma}{\Delta x}\begin{bmatrix} \sqrt{2}/_8 & \sqrt{2}/_8 \\ \sqrt{2}/_8 & \sqrt{2}/_8 \end{bmatrix}$	$\frac{\sigma}{\Delta x}\begin{bmatrix} \sqrt{2}/_4 & \sqrt{2}/_4 \\ \sqrt{2}/_4 & \sqrt{2}/_4 \end{bmatrix}$	$\frac{\sigma}{\Delta x}\begin{bmatrix} \sqrt{2}/_8 & \sqrt{2}/_8 \\ \sqrt{2}/_8 & \sqrt{2}/_8 \end{bmatrix}$
$\frac{\sigma}{\Delta x}\begin{bmatrix} 0 & 0 \\ 0 & 1/_4 \end{bmatrix}$	$\frac{\sigma}{\Delta x}\begin{bmatrix} \sqrt{5}/_{20} & \sqrt{5}/_{10} \\ \sqrt{5}/_{10} & \sqrt{5}/_5 \end{bmatrix}$	$\frac{\sigma}{\Delta x}\begin{bmatrix} \sqrt{2}/_8 & \sqrt{2}/_8 \\ \sqrt{2}/_8 & \sqrt{2}/_8 \end{bmatrix}$	

(c) Surface tension tensor $\mathbf{T}_{LG}$

(d) Surface tension force $\boldsymbol{f}^T_{st,LG}$

Figure A.6: Steps of the numerical analysis of hydrophobic wetting with the tensor-based model. Vectors are scaled by their magnitude.

Because of the direction of the spurious forces, the resulting contact angle tends to be larger for a hydrophilic surface compared to the theoretical one, while it gets smaller for a hydrophobic surface. An additional difference is that in case of hydrophilic surfaces, the spurious forces act on the gas phase, while in case of hydrophobic surfaces the liquid phase is accelerated. Since the density of the gas is lower than that of the liquid, higher velocity values may be obtained for hydrophilic surfaces.

As a consequence of the numerical issues mentioned above, the tensor based surface tension model reproduces hydrophilic and hydrophobic contact angles incorrectly. The error can be neglected around $\theta = 90°$ but gets worse as the contact angle is reduced or increased. These characteristics of the tensor-based model are shown later in Section 6.4, where wetting on flat surfaces is investigated.

References

[1] Shinan Chang et al. "Experimental and numerical study on freezing process of water droplets under surfaces with different wettability". In: *Applied Thermal Engineering* 219 (2023), p. 119516. ISSN: 1359-4311. DOI: `https://doi.org/10.1016/j.applthermaleng.2022.119516`.

[2] S. Skrna. *Simulation der Benetzung lasersrtukturierter Oberflächen mittels OpenFOAM*. Master's thesis. TU Wien, 2023.

[3] Bastian E. Rapp. "Chapter 20 - Surface Tension". In: *Microfluidics: Modelling, Mechanics and Mathematics*. Ed. by Bastian E. Rapp. Micro and Nano Technologies. Oxford: Elsevier, 2017, pp. 421–444. ISBN: 978-1-4557-3141-1. DOI: `https://doi.org/10.1016/B978-1-4557-3141-1.50020-4`.

[4] Kyowa Interface Science. *What is Surface Free Energy?* `https://www.face-kyowa.co.jp/english/en_science/en_what_surface_free_energy.html` (Accessed: 09.12.2024).

[5] Marina Ruths. "Surface Forces, Surface Tension, and Adhesion". In: *Encyclopedia of Tribology*. Ed. by Q. Jane Wang and Yip-Wah Chung. Boston, MA: Springer US, 2013, pp. 3435–3443. ISBN: 978-0-387-92897-5. DOI: `https://doi.org/10.1007/978-0-387-92897-5_463`.

[6] Frederick M. Fowkes. "Additivity of Intermolecular Forces at Interfaces. I. Determination of the Contribution to Surface and Interfacial Tensions of Dispersion Forces in Various Liquids". In: *The Journal of Physical Chemistry* 67.12 (1963), pp. 2538–2541. DOI: `https://doi.org/10.1021/j100806a008`.

[7] J Kloubek. "Calculation of surface free energy components of ice according to its wettability by water, chlorobenzene, and carbon disulfide". In: *Journal of Colloid and Interface Science* 46.2 (1974), pp. 185–190. ISSN: 0021-9797. DOI: `https://doi.org/10.1016/0021-9797(74)90001-0`.

[8] Ri Li, Nasser Ashgriz, and Sanjeev Chandra. "Maximum Spread of Droplet on Solid Surface: Low Reynolds and Weber Numbers". In: *Journal of Fluids Engineering-transactions of The Asme - J FLUID ENG* 132 (June 2010). DOI: `https://doi.org/10.1115/1.4001695`.

[9] Chris Greenshields and Henry Weller. *Notes on CFD: General Principles*. `https://doc.cfd.direct/notes/cfd-general-principles/` (Accessed: 08.02.2025).

[10] H. G. Weller et al. "A tensorial approach to computational continuum mechanics using object-oriented techniques". In: *Computer in Physics* 12.6 (Nov. 1998), pp. 620–631. ISSN: 0894-1866. DOI: `https://doi.org/10.1063/1.168744`.

[11] Fabian Rösler and Dieter Brüggemann. "Shell-and-tube type latent heat thermal energy storage: Numerical analysis and comparison with experiments". In: *Heat and Mass Transfer* 47 (Aug. 2011), pp. 1027–1033. DOI: `https://doi.org/10.1007/s00231-011-0866-9`.

[12] Constantin Zenz et al. "A compressible multiphase Mass-of-Fluid model for the simulation of laser-based manufacturing processes". In: *Computers & Fluids* 268 (2024), p. 106109. ISSN: 0045-7930. DOI: `https://doi.org/10.1016/j.compfluid.2023.106109`.

[13] Élfego Ruiz-Gutiérrez et al. "Physically consistent modelling of surface tension forces in the Volume-of-Fluid method for three or more phases". In: *Journal of Computational Physics* 513 (2024), p. 113149. ISSN: 0021-9991. DOI: `https://doi.org/10.1016/j.jcp.2024.113149`.

[14] Denis Gueyffier et al. "Volume-of-Fluid Interface Tracking with Smoothed Surface Stress Methods for Three-Dimensional Flows". In: *Journal of Computational Physics* 152.2 (1999), pp. 423–456. ISSN: 0021-9991. DOI: `https://doi.org/10.1006/jcph.1998.6168`.

[15] J.U Brackbill, D.B Kothe, and C Zemach. "A continuum method for modeling surface tension". In: *Journal of Computational Physics* 100.2 (1992), pp. 335–354. ISSN: 0021-9991. DOI: `https://doi.org/10.1016/0021-9991(92)90240-Y`.

[16] J. Volpp. "Surface tension of steel at high temperatures". In: *SN Applied Sciences* 5 (Aug. 2023). DOI: `https://doi.org/10.1007/s42452-023-05456-y`.

[17] Yancheng Zhang et al. "Numerical modelling of fluid and solid thermomechanics in additive manufacturing by powder-bed fusion: Continuum and level set formulation applied to track- and part-scale simulations". In: *Comptes Rendus Mécanique* 346.11 (2018). Computational methods in welding and additive manufacturing Simulation numérique des procédés de soudage et fabrication additive, pp. 1055–1071. ISSN: 1631-0721. DOI: `https://doi.org/10.1016/j.crme.2018.08.008`.

[18] Amanda A. Howard and Alexandre M. Tartakovsky. "A conservative level set method for N-phase flows with a free-energy-based surface tension model". In: *Journal of Computational Physics* 426 (2021), p. 109955. ISSN: 0021-9991. DOI: `https://doi.org/10.1016/j.jcp.2020.109955`.

[19] Chao Zhang and Igor Menshov. "Eulerian modelling of compressible three-fluid flows with surface tension". In: *Russian Journal of Numerical Analysis and Mathematical Modelling* 34 (Aug. 2019), pp. 225–240. DOI: `https://doi.org/10.1515/rnam-2019-0019`.

[20] Junseok Kim. “A generalized continuous surface tension force formulation for phase-field models for multi-component immiscible fluid flows”. In: *Computer Methods in Applied Mechanics and Engineering* 198.37 (2009), pp. 3105–3112. ISSN: 0045-7825. DOI: `https://doi.org/10.1016/j.cma.2009.05.008`.

[21] Chris Greenshields and Henry Weller. *Notes on CFD: General Principles - Chapter 5 Algorithms and Solvers*. `https://doc.cfd.direct/notes/cfd-general-principles/algorithms-and-solvers` (Accessed: 31.01.2025).

[22] S.T. Miller et al. “A pressure-based, compressible, two-phase flow finite volume method for underwater explosions”. In: *Computers & Fluids* 87 (2013). USNCCM Moving Boundaries, pp. 132–143. ISSN: 0045-7930. DOI: `https://doi.org/10.1016/j.compfluid.2013.04.002`.

[23] Chris Greenshields. *OpenFOAM v6 User Guide - 2.3 Breaking of a dam*. `https://doc.cfd.direct/openfoam/user-guide-v6/dambreak` (Accessed: 01.02.2025).

[24] Andreas Otto, Holger Koch, and Rodrigo Gomez Vazquez. “Multiphysical Simulation of Laser Material Processing”. In: *Physics Procedia* 39 (2012). Laser Assisted Net shape Engineering 7 (LANE 2012), pp. 843–852. ISSN: 1875-3892. DOI: `https://doi.org/10.1016/j.phpro.2012.10.109`.

[25] Asok K. Sen and Stephen H. Davis. “Steady thermocapillary flows in two-dimensional slots”. In: *Journal of Fluid Mechanics* 121 (1982), pp. 163–186. DOI: `https://doi.org/10.1017/S0022112082001840`.

[26] Douglas Kothe, Marianne Francois, and J.M. Sicilian. “Modeling of Thermocapillary Forces within a Volume Tracking Algorithm”. In: *Modeling of Casting, Welding and Advanced Solidification Processes - XI* 2 (June 2006).

[27] Z.S. Saldi. *Marangoni driven free surface flows in liquid weld pool*. PhD thesis. TU Delft, 2012.

[28] Roland Fürbacher, Gerhard Liedl, and Andreas Otto. “Fast transition from hydrophilic to superhydrophobic, icephobic properties of stainless steel samples after femtosecond laser processing and exposure to hydrocarbons”. In: *Procedia CIRP* 111 (2022). 12th CIRP Conference on Photonic Technologies [LANE 2022], pp. 643–647. ISSN: 2212-8271. DOI: `https://doi.org/10.1016/j.procir.2022.08.016`.